



*Supplement of*

## **Global nitrous oxide budget (1980–2020)**

**Hanqin Tian et al.**

*Correspondence to:* Hanqin Tian ([hanqin.tian@bc.edu](mailto:hanqin.tian@bc.edu))

The copyright of individual parts of the supplement might differ from the article licence.

## Extended methodology

### S1.1 NMIP-2: global Nitrogen/N<sub>2</sub>O Model Inter-comparison Project phase 2

The NMIP2 is a follow-up model intercomparison project of NMIP (Tian *et al.*, 2018), which provides estimates of N<sub>2</sub>O emissions from natural and agricultural soils and covers the time period 1850-2020. Eight process-based Terrestrial Biosphere Models (TBMs) participate in NMIP-2. In general, N<sub>2</sub>O emissions from soil are regulated at two levels, which are the rates of nitrification and denitrification in the soil and soil physical factors regulating the ratio of N<sub>2</sub>O to other nitrous gases (Davidson *et al.*, 2000). For N input to land ecosystems, all eight models considered N fertilizer use, atmospheric N deposition and biological fixation, but five models considered manure as N input. For vegetation processes, all models included dynamic algorithms in simulating N allocation to different living tissues and vegetation N turnover, and simulated plant N uptake using the “Demand and Supply-driven” approach. For soil N processes, all eight models simulated N leaching according to water runoff rate; however, models are different in representing nitrification and denitrification processes and the impacts of soil chemical and physical factors. The differences in simulating nitrification and denitrification processes are one of the major uncertainties in estimating N<sub>2</sub>O emissions. Model characteristics in simulating major N cycling processes associated with N<sub>2</sub>O emissions in each participating model are briefly described in Table S1.

**Table S1. Model characteristics in simulating major N cycling processes**

	CLASS IC	DLEM	ELM	ISAM	LPX-Bern	O-CN	ORCHIDEE	VISIT
Open C cycle <sup>a</sup>	Yes	Yes	Yes	Yes	Yes	Yes	Yes	Yes
C-N coupling	Yes	Yes	Yes	Yes	Yes	Yes	Yes	Yes
N pools <sup>b</sup>	(3, 1, 3)	(6,6,8)	(6,4,5)	(6,4,4)	(4,3,8)	(9,6,9)	(9,6,9)	(4,1,4)
Demand and supply-driven plant N uptake	Yes	Yes	Yes	Yes	Yes	Yes	Yes	Yes
N allocation <sup>c</sup>	Dynamic	Dynamic	Dynamic	Dynamic	Dynamic	Dynamic	Dynamic	Dynamic
Nitrification	$f(T, SWC, C_{NH4})$	$f(T, SWC, C_{NH4})$	$f(T, SWC, pH, rh, C_{NH4})$	$f(T, SWC, C_{NH4})$	$f(T, SWC, C_{NH4})$	$f(T, SWC, pH, C_{NH4})$	$f(T, SWC, pH, C_{NH4})$	$f(T, SWC, pH, C_{NH4})$
Denitrification	$f(T, SWC, C_{NO3})$	$f(T, SWC, clay, rh, C_{NO3})$	$f(T, SWC, pH, rh, C_{NO3})$	$f(T, SWC, C_{NO3})$	$f(T, SWC, R_{mb}, C_{NO3})$	$f(T, SWC, pH, R_{mb}, C_{NO3})$	$f(T, SWC, pH, denitrifier, C_{NO3})$	$f(SWC, rh, C_{NO3})$
Mineralization, immobilization	$f(C:N)$	$f(C:N)$	$f(C:N)$	$f(C:N)$	$f(C:N)$	$f(C:N)$	$f(C:N)$	$f(C:N)$
N leaching	$f(runoff, C_{NO3}, C_{NH4})$	$f(runoff, C_{NO3}, C_{NH4})$	$f(runoff, C_{NO3})$	$f(runoff, C_{NO3}, C_{NH4})$	$f(runoff, C_{NO3})$	$f(runoff, C_{NO3}, C_{NH4})$	$f(runoff, C_{NO3}, C_{NH4})$	$f(runoff, C_{NO3})$
NH <sub>3</sub> volatilization	$f(C_{NH3})$	$f(T, SWC, C_{NH3})$	No	$f(C_{NH3})$	$f(T, SWC, C_{NH3})$	$f(C_{NH3})$	$f(SWC, pH, C_{NH4})$	$f(T, SWC, C_{NH3})$

		$pH,$ $C_{NH4}$			$pH,$ $C_{NH4}$			$pH,$ $C_{NH4}$
Plant N turnover <sup>d</sup>	Dynamic	Dynamic	Dynamic	Dynamic	Dynamic	Dynamic	Dynamic	Dynamic
N resorption	Fixed	$f(C:N)$	Fixed	$f(C:N)$	Fixed	Fixed	Fixed	Fixed
N fixation	$f(N_{limit})$	$f(T,$ $SWC,$ $C_{NH4},$ $C_{NO3})$	$f(T,$ $C:N)$	$f(ET)$	Implied by mass balance	$f(N_{limit})$	Fixed	$f(ET)$
N fertilizer use	Yes	Yes	Yes	Yes	Yes	Yes	Yes	Yes
Manure N use	No	Yes	No	Yes	No	Yes	Yes	Yes
N deposition	Yes	Yes	Yes	Yes	Yes	Yes	Yes	Yes

21 <sup>a</sup> “Open” denotes that excess N can be leached from the system.

22 <sup>b</sup> Numbers of N pools (vegetation pools, litter pools, soil pools).

23 <sup>c</sup> Dynamic denotes time-varied N allocation ratio to different N pools.

24 *T*: soil temperature, *SWC*: soil water content, *clay*: soil clay fraction, *ET*: evapotranspiration, *denitrifier*:  
25 soil denitrifier biomass, *rh*: soil heterogeneous respiration, *N<sub>limit</sub>*: N limitation of vegetation growth,  
26 *C<sub>NO3</sub>*: soil  $NO_3^-$  content, *C<sub>NH4</sub>*: soil  $NH_4^+$  content.

27  
28 All NMIP2 models are driven by consistent input datasets (i.e., climate, atmospheric CO<sub>2</sub> concentration,  
29 land cover change, irrigation, atmospheric N deposition, mineral N fertilization, and manure N application  
30 and deposition) and implemented consistent simulation experiments (SH0 – SH12; Table A4). Nitrogen  
31 inputs data used in NMIP2 simulations are from History of anthropogenic Nitrogen inputs (HaNi) dataset  
32 (*Tian et al.*, 2022), which takes advantage of different data sources in a spatiotemporally consistent way to  
33 generate a set of high-resolution (5 arcminutes) gridded N input products from 1850 to 2020. HaNi data set  
34 shows that the total anthropogenic N inputs to global terrestrial ecosystems increased from 29.05 Tg N yr<sup>-1</sup>  
35 in the 1860s to 267.23 Tg N yr<sup>-1</sup> in the 2010s, with the dominant N source changing from atmospheric N  
36 deposition (before the 1900s) to manure N (the 1910s-2000s), and to synthetic fertilizer in the 2010s (Fig.  
37 B3). The climate data used to run historical simulations is the half degree CRU-JRA2.2 6-hourly forcing  
38 over 1901- 2020 (<https://catalogue.ceda.ac.uk/uuid/4bdf41fc10af4caa489b14745c665a6>). Annual CO<sub>2</sub>  
39 concentration during 1850-2020 were derived from ice core CO<sub>2</sub> data and NOAA annual  
40 observations(<https://www.esrl.noaa.gov>). Historical distribution of cropland, pasture, rangeland and  
41 irrigation during 1850-2020 were from Land-Use Harmonization 2 (LUH2) dataset (*Hurt et al.*, 2020). The  
42 original dataset of LUH2 is at a resolution of 0.25° x 0.25° longitude/latitude. We aggregated all geo-  
43 referenced input data into a consistent spatial resolution of 0.5° x 0.5° longitude/latitude to run NMIP2  
44 models.

45  
46 NMIP2 models perform a subset of 13 simulations (SH0-SH12) to quantify N<sub>2</sub>O emissions from both  
47 agricultural and natural soils during the study period, and to disentangle the effects of multiple  
48 environmental factors on soil N<sub>2</sub>O emissions. The SH1 results were taken as the “best estimates” of soil  
49 N<sub>2</sub>O emissions because they include the effects of all driving factors that models can take into account. In  
50 the SH0 simulation, driving forces were kept constant at the level in 1850 over the entire simulation period  
51 (1850-2020). According to previous N<sub>2</sub>O budget studies, atmospheric N<sub>2</sub>O growth rate and Monte-Carlo  
52 method, we suggest the following criteria for the N<sub>2</sub>O budget inclusion (Table A6), and the criteria for  
53 carbon components are consistent with TRENDY. By comparing results from factorial simulation  
54 experiments (SH0 - SH12), we attribute changes in soil N<sub>2</sub>O emissions to seven natural and anthropogenic  
55 factors, namely, climate (CLIM, including precipitation, humidity, temperature and photosynthetic active  
56 radiation changes), atmospheric CO<sub>2</sub> concentration (CO<sub>2</sub>), land cover change (LCC), irrigation (IRRI),

57 atmospheric N deposition (NDEP), mineral N fertilizer use (NFER), and manure N use in cropland  
 58 (MANN). In order to understand soil N<sub>2</sub>O emissions dynamics caused by crop cultivation, we further  
 59 separate the global and regional N<sub>2</sub>O emissions into those derived from cropland soils and those from soils  
 60 of other land ecosystems. In this study, we attribute the impact of a single factor on cropland N<sub>2</sub>O emissions.  
 61 Five models (DLEM, ISAM, O-CN, ORCHIDEE, and VISIT) considered the effects of manure N  
 62 application in cropland, therefore, we use these five models' results to calculate the manure N effect (SH1-  
 63 SH2). Meanwhile, we used results from all the eight models (i.e., CLASSIC, DLEM, ELM, ISAM, LPX-  
 64 Bern, O-CN, ORCHIDEE, and VISIT) to calculate the effects of synthetic N fertilizer use (SH1-SH3) and  
 65 atmospheric N deposition (SH1-SH4). The effect of N deposition in natural ecosystems (SH1-SH4) and the  
 66 effects of CO<sub>2</sub> (SH1-SH7) and climate (SH1-SH8) on global terrestrial ecosystems are calculated from the  
 67 eight NMIP2 models mentioned above.  
 68

69 **Table S2. Criteria for the N<sub>2</sub>O budget inclusion**

Carbon criteria	N <sub>2</sub> O criteria
(1) Steady state after spin-up, diagnosed from SH0 run: steady-state defined as an offset < 0.10 PgC yr <sup>-1</sup> , drift < 0.05 PgC yr <sup>-1</sup> per century (i.e. first is the average over 1850-2020, second is the slope x 100).	(1) Steady state after spin-up, diagnosed from SH0 run: drift < 0.2 Tg N <sub>2</sub> O-N yr <sup>-1</sup> per century (i.e. the slope x 100).
(2) Net annual land flux is a carbon sink over the 1990s and 2000s as constrained by global atmospheric and oceanic observations (Keeling & Manning, 2014), diagnosed from SH3 run.	(2) Inside the present-day (2007-2016) land emission range: 7-13 Tg N <sub>2</sub> O-N yr <sup>-1</sup> , diagnosed from SH1 run. The upper limit was calculated using the maximum total N <sub>2</sub> O emissions minus the minimum estimates of other sources, and the lower limit was calculated using the minimum total N <sub>2</sub> O emissions minus the maximum estimates of other sources. The range of total emissions was estimated by a one-box model using atmospheric N <sub>2</sub> O growth rate, and the range of the sum of other sources was calculated by a Monte-Carlo method using estimates from Tian et al. (2020).
	(3) Inside the pre-industrial land emission range: 3 to 9 Tg N <sub>2</sub> O-N yr <sup>-1</sup> , diagnosed from SH1 run. This range is derived from the pre-industrial atmospheric burden/N <sub>2</sub> O lifetime minus ocean and river/ coastal/estuary emissions (Michael J. Prather et al., 2015).

70  
71

72 **S1.2 Brief description of algorithms associated with N<sub>2</sub>O flux in each NMIP2 model:**

73 **S1.2.1: CLASSIC**

74 The representation of nitrogen cycling in CLASSIC is described in *Asaadi and Arora (2021)* and *Kou*  
 75 *Giesbrecht and Arora (2022)*. N<sub>2</sub>O production due to both nitrification and denitrification are represented.  
 76 N<sub>2</sub>O loss during nitrification ( $I_{N_2O}$ ; g N m<sup>-2</sup> d<sup>-1</sup>) is represented with the following equation:

$$77 \quad I_{N_2O} = \eta_{N_2O} f_I(T_{0.5}) f_I(\psi) N_{NH_4} \quad (1)$$

78  $\eta_{N_2O}$  is a coefficient (d<sup>-1</sup>),  $f_I(T_{0.5})$  is a dimensionless scalar that depends on soil temperature averaged over  
 79 the top 0.5m soil depth ( $T_{0.5}$ ),  $f_I(\psi)$  is a dimensionless scalar that depends on soil matric potential ( $\psi$ ), and  
 80  $N_{NH_4}$  is the soil ammonium pool (g N m<sup>-2</sup>).

81 N<sub>2</sub>O loss during denitrification ( $E_{N_2O}$ ; g N m<sup>-2</sup> d<sup>-1</sup>) is represented with the following equation:

$$E_{N_2O} = \mu_{N_2O} f_E(T_{0.5}) f_E(\theta) N_{NO_3} \quad (2)$$

$\mu_{N_2O}$  is a coefficient ( $d^{-1}$ ),  $f_E(T_{0.5})$  is a dimensionless scalar that depends on soil temperature averaged over the top 0.5m soil depth ( $T_{0.5}$ ),  $f_E(\theta)$  is a dimensionless scalar that depends on soil moisture ( $\theta$ ), and  $N_{NO_3}$  is the soil nitrate pool ( $g\ N\ m^{-2}$ ).

86  
87

### S1.2.2: DLEM

88 The nitrogen cycle scheme in DLEM2.0 (Xu et al., 2017; Yang et al., 2015; Tian et al. 2020) are similar as  
89 DLEM1.0 (Lu and Tian, 2013; Tian et al., 2012b; Tian et al., 2010; Tian et al., 2011; Xu et al., 2011),  
90 However, the  $N_2O$  emission schemes in DLEM2.0 (Xu et al., 2017) have been modified based on Chatskikh  
91 et al. (2005) and Heinen (2006).

92

$$R_{nit} = k_{nit\_max} f(T1) f(WFPS) C_{NH_4} \quad (3)$$

94

$$R_{den} = k_{den\_max} f(T2) f(WFPS) C_{NO_3} \quad (4)$$

96

97 where  $R_{nit}$  is the daily nitrification rate ( $g\ N/m^2/d$ );  $R_{den}$  is the daily denitrification rate ( $g\ N/m^2/d$ );  
98  $f(T1)$  and  $f(T2)$  are the impact function of daily soil temperature on nitrification and denitrification,  
99 respectively;  $f(WFPS)$  is the impact function of water-filled pore space (WFPS) on nitrification,  
100 denitrification and  $N_2O$  diffusion;  $k_{nit\_max}$  is the maximum fraction of  $NH_4^+$ -N that is converted to  $NO_3^-$ -  
101 N or gases (0-1);  $k_{den\_max}$  is the maximum fraction of  $NO_3^-$ -N that is converted to gases (0-1);  $C_{NH_4}$  and  
102  $C_{NO_3}$  are the soil  $NH_4^+$ -N and  $NO_3^-$ -N content ( $g\ N/m^2$ ).  $N_2O$  from denitrification and nitrification processes  
103 are calculated as,

104

$$R_{N_2O} = (R_{nit} + R_{den}) f(T3) (1 - f(WFPS)) \quad (5)$$

106

107 where  $R_{N_2O}$  is the daily  $N_2O$  emission rate ( $g\ N/m^2/d$ );  $f(T3)$  is the impact function of daily soil  
108 temperature on  $N_2O$  diffusion rate from soil pores. The calculation methods for these functions and  
109 parameters were described in detail in Xu et al. (2017) and Yang et al. (2015).

110

### S1.2.3: ELM

112 The nitrogen dynamics in ELM is simulated based on the theory of equilibrium chemistry approximation  
113 (Zhu et al., 2016). Plants, soil microbes, and abiotic factors such as mineral surfaces coexist in the same  
114 soil environment and vie for a diverse array of nutrients, including  $NH_4^+$ ,  $NO_3^-$ . Due to the limited  
115 availability of these nutrients, intense competitive interactions are expected. The competition of those  
116 limited resources is represented by consumer–substrate networks, therefore, the uptake of nutrient substrate  
117 by each consumer is dependent on the relative competitiveness of one consumer over the others. Nutrient  
118 consumers' competitiveness is parametrized with kinetic parameters (Zhu et al., 2016). As a result, neither  
119 plant nor soil microbes get the first priority to access nutrient substrates. Instead, when the potential nutrient  
120 demands (from all nutrient consumers) exceed the supply at a given time step, the allocation of limited  
121 nutrients among the consumers affects their performance (e.g., plant growth, soil organic matter  
122 accumulation, nitrification, denitrification rates). ELM adopts a multiple-consumer-multiple-substrate  
123 competition network (Zhu et al., 2016; Zhu et al., 2019) to simulate (1) nitrogen uptake facilitated by  
124 nitrogen carrier enzymes, (2) binding of a nutrient substrate to a particular enzyme precludes it from  
125 attaching to other enzymes, and (3) rates and affinities of consumers for different substrates. After the  
126 nutrient competition has been resolved, scaling terms ( $f(ECA_{nit})$  and  $f(ECA_{den})$ ) will be applied to the  
127 potential nitrification and denitrification processes:

128

$$R_{nit} = k_{nit\_max} f(\theta) f(T) (1 - f(O)) f(ECA_{nit}) C_{NH_4} \quad (6)$$

130

$$R_{den} = \min(f(deomp), f(C_{NO3}))f(ECA_{den}) \quad (7)$$

where  $k_{nit,max}$  is the maximum nitrification rate,  $f(\theta)$ ,  $f(T)$ ,  $f(O)$  are soil moisture, temperature, and oxygen scalars, respectively.  $f(deomp)$  and  $f(C_{NO3})$  are carbon limited and NO<sub>3</sub>- limited denitrification rates (Del Grosso et al., 2000).

#### 137 S1.2.4: ISAM

138 ISAM model contains detailed calculations of the terrestrial ecosystem's organic and mineral N cycle (Yang  
139 et al., 2009). The major N processes in ISAM include biological fixation, leaching, mineralization and  
140 immobilization, plant uptake, nitrification, and denitrification. The soil biogeochemistry module of ISAM  
141 shares the same ten soil layers (to 3.5 m depth) as the soil biogeophysics and calculates the vertical transport  
142 of SOC and N (Shu et al., 2020; Yang et al., 2009). N<sub>2</sub>O emission in ISAM N<sub>2</sub>O is produced as a byproduct  
143 of nitrification and denitrification (Xu et al., 2021). N<sub>2</sub>O module explicitly accounts for the vertical transport  
144 of C, N, and O<sub>2</sub> within every soil layer for both saturated and unsaturated soil conditions by accounting for  
145 the process of oxygen diffusing into the soil from the atmosphere and the soil oxygen supply. The model  
146 also explicitly accounts for the effects of anoxic and oxic environments on nitrification (N<sub>ni</sub>, Eq. 6) and  
147 denitrification (N<sub>de</sub>, Eq. 7). Both environments are calculated based on the fraction of anoxic soil depending  
148 on soil O<sub>2</sub> concentration, which is non-linearly correlated with the chemical pathways forming N<sub>2</sub>O.

$$149 N_{ni} = NH_4^+ \times (1 - e^{-F_{te,m} \times F_{sm,m} \times r_{ni}}) \times F_{pH,m,ni} \times R_d \quad (8)$$

$$150 N_{de} = NO_3^- \times r_{de} \times Rh \times F_{pH,m,de} \times R_d \quad (9)$$

151 where  $NH_4^+$  and  $NO_3^-$  are ammonium and nitrate pool sizes;  $F_{te,m}$  is temperature modifier;  $F_{sm,m}$  is soil  
152 moisture modifier;  $r_{ni}$  and  $r_{de}$  are base nitrification and denitrification rates;  $F_{pH,m,ni}$  and  $F_{pH,m,de}$  are pH  
153 modifiers for nitrification and denitrification;  $R_d$  is relative soil anoxic fraction;  $Rh (= 1 - R_d)$  is heterotrophic  
154 respiration.

155 Under anoxic soil conditions, N<sub>2</sub>O is produced through denitrification, while under oxic soil conditions,  
156 more N<sub>2</sub>O is produced from nitrification. The model accounts for soil NH<sub>4</sub><sup>+</sup> volatilization at the soil surface  
157 when NH<sub>4</sub><sup>+</sup> in NH<sub>4</sub><sup>+</sup>-containing fertilizers (e.g., urea) is converted to ammonia gas, depending upon pH  
158 (Huang and Gerber, 2015). The soil NH<sub>4</sub><sup>+</sup> volatilization in the model is also affected by the anoxic condition,  
159 which increases under a higher temperature and relatively lesser soil anoxic condition. The model accounts  
160 for the impacts of pH on nitrification, denitrification, and volatilization rates (Li et al., 2000; Xu-Ri and  
161 Prentice, 2008). We prescribe the soil pH from the Global Soil Dataset for Earth System Modeling dataset  
162 (GSDE) (Shangguan et al., 2014).

#### 163 S1.2.5: LPX-Bern

164 The implementation of nitrogen dynamics in LPX-Bern is based on the work of Xu-Ri and Prentice (2008).  
165 Nitrogen uptake by plants is governed by their demand and the availability of nitrogen in two soil pools  
166 representing ammonium and nitrate. Nitrogen from deposition and fertilization are added to these inorganic  
167 soil pools. Losses include ammonium volatilization, nitrate leaching as well as N<sub>2</sub>O and NO production  
168 during nitrification and N<sub>2</sub>O, NO and N<sub>2</sub> production during denitrification. Aerobic nitrification of  
169 ammonium is dependent on soil temperature ( $T_{soil}$ ) and indirectly on soil water content due to the  
170 partitioning of wet and dry soil:

$$171 R_{nit} = \max_{nit} f_1(T_{soil}) C_{NH4,dry} \quad (10)$$

172 where  $\max_{nit} = 0.92 \text{ day}^{-1}$  is the daily maximum nitrification rate at 20°C.

180 Anaerobic denitrification of nitrate in wet soil depends on labile carbon availability and soil temperature:

$$181 R_{den} = R_{mb}/(R_{mb} + K_{mb})f_2(T_{soil})C_{NO3,wet}/(C_{NO3,wet} + K_n) \quad (11)$$

183 The parameters  $K_{mb}$  and  $K_n$  are taken from *Xu-Ri and Prentice* (2008) and  $R_{mb}$  is the microbiological soil  
185 respiration. The amount of nitrogen lost as  $N_2O$  due to nitrification and denitrification is modelled as a  
186 function of soil temperature, water content and the respective process rate.

### 187 **S1.2.6: O-CN**

188 The treatment of inorganic soil nitrogen dynamics in O-CN follows largely *Xu-Ri and Prentice* (2008). O-  
189 CN (*Zaehle and Friend*, 2010) considers N losses to  $NH_3$  volatilisation,  $NO_x$ ,  $N_2O$  and  $N_2$  production and  
190 emission, as well as  $NH_4$  and  $NO_3$  leaching. Inorganic nitrogen dynamics in the soil are tightly coupled to  
191 plant uptake and net mineralization. The anaerobic volume fraction of the soil is estimated by an empirical  
192 function of the fractional soil moisture content (*Zaehle et al.*, 2011). The fraction of ammonium in the  
193 aerobic part of the soil is subject to nitrification, according to:

$$194 R_{nit} = v_{max_{nit}}f(T1)f(pH1)C_{NH4} \quad (12)$$

195 where  $f(pH1)$  is the soil pH response functions for nitrification (*Li et al.*, 1992; *Xu-Ri and Prentice*, 2008),  
196 and  $v_{max_{nit}}$  is the maximum daily nitrification rate under 20°C and favourable pH conditions (*Xu-Ri and*  
197 *Prentice*, 2008).

200 Gross denitrification of the fraction of nitrate under anoxic conditions is modelled as:

$$201 R_{den} = R_{mb}/(R_{mb} + K_{mb})f(T2)f(pH2)C_{NO3}/(C_{NO3} + K_n) \quad (13)$$

202 where  $f(pH2)$  is the soil pH response functions for denitrification (*Li et al.*, 1992; *Xu-Ri and Prentice*, 2008),  
203  $R_{mb}$  is the soil microbial respiration rate, and  $K_{mb}$  and  $K_n$  parameters taken from *Li et al.* (1992).

204 The  $N_2O$  production from nitrification and denitrification is then calculated as:

$$205 R_{N2O} = a_{nit}f(T1)R_{nit} + b_{den}f(T2)f(pH3)R_{den} \quad (14)$$

206 where  $a_{nit}$  and  $b_{den}$  are fraction loss constants,  $f(pH3)$  is a pH-modifier changing the degree of denitrification  
207 producing  $N_2O$  versus  $NO_x$  or  $N_2$  (*Zaehle et al.*, 2011). Emissions of volatile compounds are simulated  
208 using the empirical emission of *Xu-Ri and Prentice* (2008).

### 209 **S1.2.7: ORCHIDEE**

210 Modeling of the mineral N dynamics by the ORCHIDEE model originates from the formulations used in  
211 the O-CN (*Zaehle and Friend*, 2010). It is composed of five pools for ammonium/ammoniac, nitrate,  $NO_x$ ,  
212 nitrous oxide, and di-nitrogen forms.  $N_2O$  production in both nitrification and denitrification processes are  
213 represented.

214 The potential daily rate of nitrification,  $R_{nit}$ , occurs only on the aerobic fraction of the soil and is a function  
215 of temperature, pH, and ammonium concentration ( $C_{NH4}$ ):

$$216 R_{nit} = (1 - f(WFPS))f(T1)f(pH1)k_{nit}C_{NH4} \quad (15)$$

217 where  $k_{nit}$  is the reference potential  $NO_3^-$  production per mass unit of ammonium.

## 230 S1.2.8: VISIT

231 The nitrogen cycle scheme of VISIT is composed of three organic soil nitrogen pools (microbe, litter, and  
232 humus), two inorganic soil nitrogen pools (ammonium and nitrate), and vegetation pools. Fertilizer is  
233 considered as an input to the ammonium and nitrate pools at a fixed ratio, and manure as an input into the  
234 litter organic nitrogen pool. N<sub>2</sub>O emissions through nitrification and denitrification are estimated using the  
235 scheme developed by *Parton et al.* (1996). Nitrification-associated N<sub>2</sub>O emission ( $R_{nit,N_2O}$ ) is evaluated as  
236 follows,

$$237 R_{nit,N_2O} = f(WFPS)f(pH1)f(T1)(K_{max} + F_{max}f(NH_4)) \quad (16)$$

239 where  $K_{max}$  is the soil-specific turnover coefficient;  $F_{max}$  is the parameter of maximum nitrification gas flux;  
240 and  $f(NH_4)$  is the effect of soil ammonium on nitrification. Denitrification-associated N<sub>2</sub>O emission  
241 ( $R_{den,N_2O}$ ) is evaluated by the following equation:

$$242 R_{den,N_2O} = R_{den}(1 + R_{N_2/N_2O}) \quad (17)$$

$$243 R_{den} = \min(f(NO_3), f(CO_2)) \times f(WFPS) \quad (18)$$

247 where  $R_{N_2/N_2O}$  is the fractionation coefficient, which is also a function of WFPS, soil nitrate, and  
248 heterotrophic respiration,  $f(NO_3)$  is the maximum denitrification rate in high soil respiration rate condition,  
249  $f(CO_2)$  is the maximum denitrification rate in high NO<sub>3</sub><sup>-</sup> levels, and  $f(WFPS)$  is the effect of WFPS on  
250 denitrification rate.

251 N<sub>2</sub>O production by nitrification ( $R_{N_2O,nit}$ , g N-N<sub>2</sub>O/m<sup>2</sup>/d) is expressed as a function of the potential daily rate  
252 of nitrification ( $R_{nit}$ , g N-NO<sub>3</sub><sup>-</sup>/m<sup>2</sup>/d), temperature and the water content as shown in *Zhang et al.* (2002).

$$253 R_{N_2O,nit} = f(WFPS)f(T1)R_{nit}p_{N_2O,nit} \quad (19)$$

254 where  $p_{N_2O,nit}$  (g N-N<sub>2</sub>O (g N-NO<sub>3</sub><sup>-</sup>)<sup>-1</sup>) is the reference N<sub>2</sub>O production per mass unit of NO<sub>3</sub><sup>-</sup> produced by  
255 nitrification. The denitrification occurs on the anaerobic fraction of the soil which is computed as a function  
256 of the water-filled porosity ( $f(WFPS)$ ) and is controlled by temperature, pH, soil NO concentration and  
257 denitrifier microbial activity ( $a_{microb}$ , g m<sup>-2</sup>) (*Li et al.*, 2000).

$$258 R_{N_2O,den} = f(WFPS)f(T2)f(pH)f(NO)p_{N_2O,den}a_{microb} \quad (20)$$

259 where  $f(NO)$  is a Michaelis-Menten shape function and  $p_{N_2O,den}$  is the reference N<sub>2</sub>O production per mass  
260 unit of denitrifier microbes.

## 261 S2 The FAOSTAT inventory

262 The FAOSTAT emissions data (*FAO*, 2022) are computed at Tier 1 following *IPCC* (2006), Vol. 4. The  
263 overall equation is as follows:

264 Direct emissions are estimated at the country level, using the formula:

$$265 Emission = A * EF \quad (21)$$

266 where emission represents kg N yr<sup>-1</sup>;  $A$  represents the amount of N in the following items (annual synthetic  
267 N applications/manure applied to soils/manure left on pasture/manure treated in manure management  
268 systems/crop residue/biomass burned amount) in kg N yr<sup>-1</sup>;  $EF$  = Tier 1, default IPCC emission factors,  
269 expressed in kg N/kg N.



279  
280 Indirect emissions are estimated at the country level, using the formula:

281  
282 
$$Emission = A_{v\&l} * EF \quad (22)$$

283  
284 where emission represents kg N yr<sup>-1</sup>;  $A_{v\&l}$  represents the fraction of manure/synthetic N fertilizers that  
285 volatilize as NH<sub>3</sub> and NO<sub>x</sub> and are lost through runoff and leaching in kg N yr<sup>-1</sup>;  $EF$  = Tier 1, default IPCC  
286 emission factors, expressed in kg N/kg N.

287  
288 Synthetic N fertilizers: N<sub>2</sub>O from synthetic fertilizers is produced by microbial processes of nitrification  
289 and denitrification taking place on the addition site (direct emissions), and after volatilization/redeposition  
290 and leaching processes (indirect emissions).

291  
292 Manure management: The term manure includes both urine and dung (i.e., both liquid and solid material)  
293 produced by livestock. N<sub>2</sub>O is produced directly by nitrification and denitrification processes in the manure,  
294 and indirectly by nitrogen (N) volatilization and redeposition processes.

295 Manure applied to soils: N<sub>2</sub>O is produced by microbial processes of nitrification and denitrification taking  
296 place on the application site (direct emissions), and after volatilization/redeposition and leaching processes  
297 (indirect emissions).

298  
299 Manure left on pastures: N<sub>2</sub>O is produced by microbial processes of nitrification and denitrification taking  
300 place on the deposition site (direct emissions), and after volatilization/redeposition and leaching processes  
301 (indirect emissions).

302  
303 Crop Residue: N<sub>2</sub>O emissions from crop residues consist of direct and indirect emissions from nitrogen (N)  
304 in crop residues left on agricultural fields by farmers and from forages during pasture renewal (following  
305 the definitions in the IPCC guidelines (IPCC, 2006)). Specifically, N<sub>2</sub>O is produced by microbial processes  
306 of nitrification and denitrification taking place on the deposition site (direct emissions), and leaching  
307 processes (indirect emissions).

308  
309 Cultivation of organic soils: The FAOSTAT domain “Cultivation of organic soils” contains estimates of  
310 direct N<sub>2</sub>O emissions associated with the drainage of organic soils – histosols – under cropland and grazed  
311 grassland.

312  
313 Burning-savanna: N<sub>2</sub>O emissions from the burning of vegetation biomass in the land cover types: Savanna,  
314 Woody Savanna, Open Shrublands, Closed Shrublands, and Grasslands. Burning-crop residues: N<sub>2</sub>O  
315 produced by the combustion of a percentage of crop residues burnt on-site. Burning-biomass: N<sub>2</sub>O  
316 emissions from the burning of vegetation biomass in the land cover types: Humid tropical forests, other  
317 forests, and organic soils.

### 318 319 **S3 The EDGAR v7.0 inventory**

320 The new online version, EDGAR v7.0 ([https://edgar.jrc.ec.europa.eu/dataset\\_ghg70](https://edgar.jrc.ec.europa.eu/dataset_ghg70)) incorporates a full  
321 differentiation of emission processes with technology-specific emission factors and additional end-of-pipe  
322 abatement measures and as such updates and refines the emission estimates. The emissions are modelled  
323 based on the latest scientific knowledge and available global statistics primarily from International Energy  
324 Agency (IEA, 2021) for energy related sectors, FAO statistics (FAO, 2022) for agriculture, which were  
325 complemented for the rest of sectors with United States Geological Survey (USGS), International Fertiliser  
326 Association (IFA), Gas Flaring Reduction Partnership (GGFR)/U.S. National Oceanic and Atmospheric  
327 Administration (NOAA) and World Steel Association (worldsteel) recent statistics; the methods are those  
328 recommended by IPCC (2006). Official data submitted by the Annex I countries to the United Nations

329 Framework Convention on Climate Change (UNFCCC) and to the Kyoto Protocol are used to some extent,  
330 particularly regarding control measures implemented since 1990 that are not described by international  
331 statistics. A fast-Track approach was used to extend the N<sub>2</sub>O emission time series for the latest years up to  
332 2021 (Crippa *et al.*, 2021; Crippa *et al.*, 2022).

333  
334 The N<sub>2</sub>O emission factors for direct soil emissions of N<sub>2</sub>O from the use of synthetic fertilizers, from manure  
335 used as fertilizers, and from crop residues are taken from *IPCC* (2006), which updated the default IPCC  
336 emission factor in the IPCC Good Practice Guidance (2000) with a 20% lower value. N<sub>2</sub>O emissions from  
337 the use of animal waste as fertilizer are estimated considering both the loss of N that occurs from manure  
338 management systems before manure is applied to soils and the additional N introduced by bedding material  
339 (Janssens-Maenhout *et al.*, 2019). N<sub>2</sub>O emissions from fertilizer use and CO<sub>2</sub> from urea fertilization are  
340 estimated based on IFA and FAO recent statistics.

341  
342 N<sub>2</sub>O emissions from manure management are based on the distribution of manure management systems  
343 from Annex I countries reporting to the UNFCCC, Zhou *et al.* (2007) for China and *IPCC* (2006) for the  
344 rest of the countries.

345  
346 Different N<sub>2</sub>O emission factors are applied to tropical and non-tropical regions. N and dry matter content  
347 of agricultural residues are estimated from the cultivation area and yield for 24 crop types from *FAO* (2022)  
348 and using emission factors of *IPCC* (2006).

349  
350 Indirect N<sub>2</sub>O emissions from leaching and runoff of nitrate are estimated from N input to agricultural soils.  
351 Leaching and runoff are assumed to occur in all agricultural areas except non-irrigated dryland regions,  
352 which are identified with maps of FAO Geonetwork (<https://www.fao.org/land-water/databases-and-software/geonetwork/en/>). The fraction of N lost through leaching and runoff is based on the study of Van  
353 Drecht *et al.* (2003). The updated emission factor for indirect N<sub>2</sub>O emissions from N leaching and run-off  
354 from the *IPCC* (2006) guidelines is selected, while noting that it is 70% lower than the mean value of the  
355 1996 IPCC Guidelines and the IPCC Good Practice Guidance *IPCC* (1996; 2000).

356  
357 Indirect N<sub>2</sub>O emissions from atmospheric deposition of N of NO<sub>x</sub> and NH<sub>3</sub> emissions from non-agricultural  
358 sources, mainly fossil fuel combustion, are estimated using N in NO<sub>x</sub> and NH<sub>3</sub> emissions from these sources  
359 as activity data, based on EDGAR v7.0 database for these gases. The same emission factor from *IPCC*  
360 (2006) is used for indirect N<sub>2</sub>O from atmospheric deposition of N from NH<sub>3</sub> and NO<sub>x</sub> emissions, as for  
361 agricultural emissions (Janssens-Maenhout *et al.*, 2019).

362  
363 The uncertainties for EDGAR N<sub>2</sub>O emissions estimated by Solazzo *et al.* (2021) are based primarily on the  
364 uncertainties in emissions factors and activity data statistics from the *IPCC* (2006). Globally, these  
365 emissions are accurate within an interval of ±113 for energy, -12% to +16% for industrial processes and  
366 product use, -225 to +302 for agriculture, -159% to 203% for waste and ±112% for others; the most  
367 uncertain emissions are those related to N<sub>2</sub>O from waste and agriculture.

#### 368 369 370 **S4 The UNFCCC inventory (need description of UNFCCC)**

371 The UNFCCC collects detailed data on GHG emissions from its parties. Following extensive guidance  
372 developed by IPCC (Buendia *et al.*, 2019; Eggleston *et al.*, 2006), parties to the convention prepare national  
373 GHG inventories, including emissions (and sinks) of N<sub>2</sub>O. All anthropogenic activities are covered, in  
374 agriculture both direct and indirect N<sub>2</sub>O emissions are included. While IPCC basically provides emission  
375 factor approaches, parties are encouraged to take account of national specificities, use national factors and  
376 data, wherever available, or develop emission models, with adequate scientific proof provided.  
377 Combustion-related emissions and emissions from industrial processes may take advantage of emission

378 monitoring or specific plant operation conditions, if provided. Emission processes that are not associated  
 379 with anthropogenic activities are also not covered in the inventories.

380  
 381 Obligations and quality of data provided differ strongly by country category. High scrutiny is put on GHG  
 382 inventories from countries listed in Annex-I of the convention (Annex-I countries include most European  
 383 countries, U.S. and Canada, Australia and New Zealand, and Japan). Annex-I countries are obliged to  
 384 provide annual national inventories in considerable detail and have to be very transparent also in terms of  
 385 methodology used and underlying information. Each year, time-series of emissions and underlying data  
 386 since 1990 (in a few cases, alternative base years are used) up to the pre-previous year are freshly provided  
 387 in April each year (e.g., in April 2023 data up to the year 2021 had to be provided), leading to a  
 388 homogeneous data series. Reports and emission data are provided (to UNFCCC, and to all users from the  
 389 UNFCCC web site at <https://unfccc.int/reports>) in standardized format such that they can be transferred to  
 390 databases. National results are routinely being checked and evaluated by expert teams in form of specific  
 391 internal and external audits to assure data quality and consistency.

392  
 393 National information is highly relevant also for non-Annex I countries to the UNFCCC and is being  
 394 collected and distributed by UNFCCC as well. Requirements are much less stringent, however, as parties  
 395 are expected to provide data only according to their own capabilities and the support they get from other  
 396 countries. The so-called Biannual Update Reports are to be prepared every other year only. While in  
 397 principle following the same IPCC guidance, commitments to format, timing, and quality assessment are  
 398 by far less stringent, and the own ambition level of the respective party (country) may determine much of  
 399 the outcome. In any case, self-reporting of a country always also means the party is willing to take the  
 400 responsibility of the emissions reported.

401  
 402 The “EDGAR/UNFCCC” dataset used in this paper utilizes the database for Annex-I countries for  
 403 emissions from fossil-fuel consumption, industrial processes, waste and wastewater, and merges with the  
 404 respective set derived from EDGARv7.0 for all remaining countries.

### 405 406 **S5.1 The SRNM model: Flux upscaling model**

407 The SRNM model (Wang et al., 2020) was applied to simulate direct cropland-N<sub>2</sub>O emissions. In SRNM,  
 408 N<sub>2</sub>O emissions were simulated from N application rates using a quadratic relationship, with spatially  
 409 variable model parameters that depend on climate, soil properties, and management practices. The original  
 410 version of SRNM was calibrated using field observations only from China (Zhou et al., 2015). In this study,  
 411 we used the global N<sub>2</sub>O observation dataset to train it to create maps of gridded annual emission factors of  
 412 N<sub>2</sub>O and the associated emissions at 5-minute resolution from 1901 to 2014 (Cui et al., 2021). The gridded  
 413 EF and associated direct cropland-N<sub>2</sub>O emissions are simulated based on the following equation:

414  
 415

$$416 \quad E_{ijt} = \alpha_{ij} N_{ijt}^2 + \beta_{ij} N_{ijt} + \varepsilon_{ijt}, \quad \forall i \tag{23}$$

417 where

$$418 \quad \alpha_{ij} \sim N\left(\sum_k (x_k \lambda_{ijk}), \sigma_{ijk}^2\right), \quad \beta_{ij} \sim N\left(\sum_k (x_k \phi_{ijk}), \sigma_{ijk}^{\prime 2}\right) \tag{24}$$

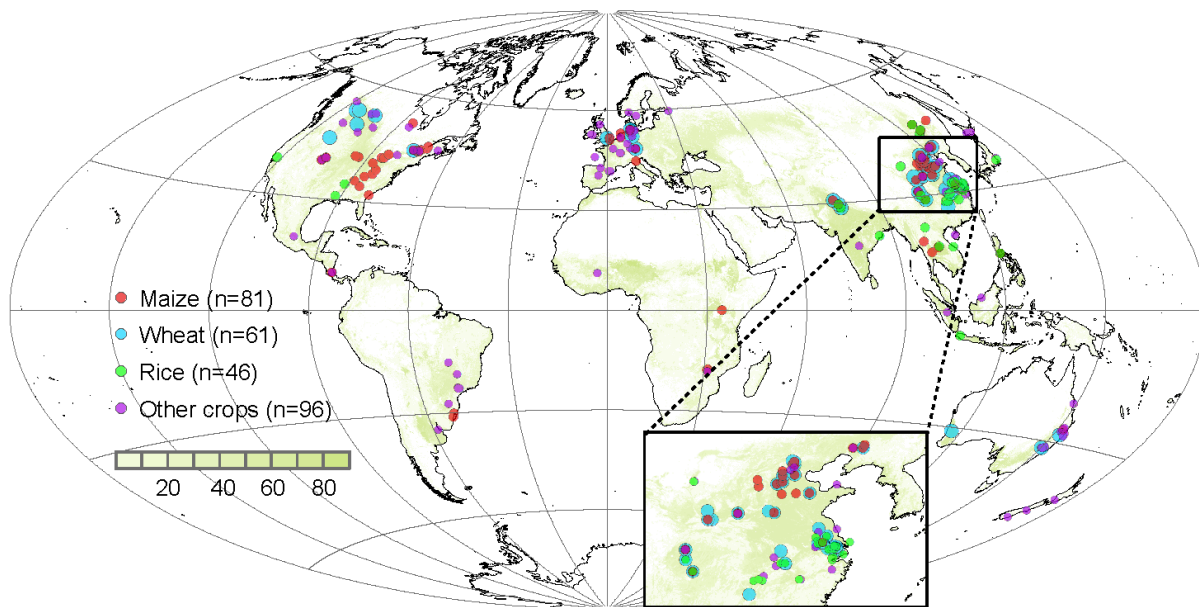
$$419 \quad \lambda_{ijk} \sim N(\mu_{ijk}, \omega_{ijk}^2), \quad \phi_{ijk} \sim N(\mu'_{ijk}, \omega_{ijk}^{\prime 2}), \quad \varepsilon_{ijt} \sim N(0, \tau^2) \tag{25}$$

420 and  $i$  denotes the sub-function of N<sub>2</sub>O emission ( $i=1, 2, \dots, I$ ) that applies for a sub-domain division  $W_i$  of  
 421 six climate or soil factors,  $j$  represents the type of crop ( $j=1-2$ , 1 for upland crops and 2 for paddy rice),  $k$  is  
 422 the index of climate or soil factors ( $k=1-6$ , i.e., soil pH, clay content, SOC, BD, the sum of cumulative  
 423 precipitation and irrigation, mean daily air temperature).  $W_i$  denotes a set of the range of multiple  $x_k$ .  $E_{ijt}$

424 denotes direct N<sub>2</sub>O emission flux (kg N ha<sup>-1</sup> yr<sup>-1</sup>) estimated for crop type  $j$  in year  $t$  in the  $i$ th sub-domain,  
425  $N_{ijt}$  is N application rate (kg N ha<sup>-1</sup> yr<sup>-1</sup>), and  $a_{ij}$  and  $b_{ij}$  are defined as summation of the product of  $x_k$  and  $l_{ijk}$   
426 over  $k$ . The random terms  $l$  and  $f$  are assumed to be independent and normally distributed, representing the  
427 sensitivity of  $a$  and  $b$  to  $x_k$ .  $e$  is the model error.  $m$  and  $m\phi$  are the mean effect of  $x_k$  for  $a$  and  $b$ , respectively.  
428  $s$ ,  $s\phi$ ,  $w$ ,  $w\phi$ , and  $t$  are standard deviations. Optimal sub-domain division, associated parameters mean  
429 values and standard deviations were determined by using the Bayesian Recursive Regression Tree version  
430 2 (BRRT v2), constrained by the extended global cropland-N<sub>2</sub>O observation dataset. The detailed  
431 methodological approach of the BRRT v2 is described by Zhou et al (2015).  
432

## 433 **S5.2 Global cropland N<sub>2</sub>O observation dataset**

434 We aggregated cropland N<sub>2</sub>O flux observation data from 180 globally distributed observation sites from  
435 online databases, on-going observation networks, and peer-reviewed publications (Figure S1). Chamber-  
436 based observations were only included in this dataset. These data repositories are as follows: the  
437 NitroEurope, CarbonEurope, GHG-Europe (EU-FP7), GRACenet, TRAGnet, NANORP, and 14 meta-  
438 analysis datasets (Decock, 2014; Harris et al., 2014; Helgason et al., 2005; Hénault et al., 2005; Hickman  
439 et al., 2014; Kim et al., 2013a; Kim et al., 2013b; Lehuger et al., 2011; Leppelt et al., 2014; Rochette and  
440 Janzen, 2005; Sacks et al., 2010; Shcherbak et al., 2014; Stehfest and Bouwman, 2006; Walter et al., 2015).  
441 Four types of data were excluded from our analysis: (i) observations without a zero-N control for  
442 background N<sub>2</sub>O emission, (ii) observations from sites that used controlled-release fertilizers or nitrification  
443 inhibitors, (iii) observations not covering the entire crop growing season, (iv) observations made in  
444 laboratory or greenhouse. We then calculated cropland-N<sub>2</sub>O emissions as the difference between observed  
445 N<sub>2</sub>O emission ( $E$ ) and background N<sub>2</sub>O emission ( $E_0$ ). Values of EF were estimated for each nonzero N  
446 application rate ( $N_a$ ) as direct cropland-N<sub>2</sub>O emission divided by  $N_a$ :  $EF = (E - E_0)/N_a$ . This yielded a  
447 global dataset of direct cropland-N<sub>2</sub>O emissions, N-rate-dependent N<sub>2</sub>O EFs and fertilization records from  
448 each site (i.e., 1,052 estimates for upland crops from 152 sites and 154 estimates for paddy rice from 28  
449 sites), along with site-level information on climate, soils, crop type, and relevant experimental parameters.  
450 Total numbers of sites and total measurements in the dataset were more than doubled those for previous  
451 datasets of N<sub>2</sub>O EF. The extended global N<sub>2</sub>O observation network covered most of fertilized croplands,  
452 representing a wide range of environmental conditions globally. For each site in our dataset, the variables  
453 included four broad categories: N<sub>2</sub>O emissions data, climate data (cumulative precipitation and mean daily  
454 air temperature), soil attributes (soil pH, clay content, SOC, BD), and management-related or experimental  
455 parameters (N application rate, crop type). More details on global cropland N<sub>2</sub>O observation dataset can be  
456 found in Cui et al. (2021).  
457



458  
 459 **Figure S1 Global observation dataset of N<sub>2</sub>O EF for direct soil emissions.** Green area indicates the  
 460 harvested areas of all crops derived from the Earthstat. Sites are indicated in different colors for maize,  
 461 wheat, rice, and other crops.  
 462

463 **S5.3 Gridded input datasets:**

464 The updated SRNM model was driven by many input datasets, including climate, soil properties,  
 465 agricultural management practices (e.g., fertilization, tillage, irrigation), as well as the historical distribution  
 466 of cropland. Cumulative precipitation and mean daily air temperature over the growing season were  
 467 acquired from the CRU TS V4.06 climate dataset (0.5-degree resolution) (Harris *et al.*, 2014), where  
 468 growing season in each grid cell was identified following Sacks *et al.* (2010) The patterns of SOC, clay  
 469 content, BD, and soil pH were acquired from the HWSD v1.2 ((Berdanier and Conant, 2012), 1-km  
 470 resolution). Both climate and soil properties were re-gridded at 5-arc-minute spatial resolution using a first-  
 471 order conservative interpolation widely used in the CMIP5 model intercomparison (Yang *et al.*, 2017). The  
 472 annual cropland area at 5-arc-minute spatial resolution from 1961 to 2020 was obtained from the History  
 473 Database of the Global Environment (HYDE 3.2.1) (Goldewijk *et al.*, 2017).  
 474

475 For fertilization, crop-specific N fertilizer inputs (including synthetic N fertilizers, crop residues and  
 476 manure), fertilizer types, and placement during 1961-2020 were obtained from Adalibieke *et al.*, (2023).  
 477 The frequency (i.e., one or multiple times) of N fertilization were the same as Cui *et al.* (2021) and we  
 478 assumed that the frequency remained constant during the study period. For tillage, the fraction of tillage by  
 479 crop during 1961-2020 was obtained from Adalibieke *et al.*, (2023), which was constructed with the country  
 480 and province (or state) level no-tillage area data during 1961-2020 and downscaled to grid with the method  
 481 of Porwollik *et al.* (2019). For irrigation, the History Database of the Global Environment (HYDE version  
 482 3.2) (Goldewijk *et al.*, 2017) and the MIRCA2000 dataset (Portmann *et al.*, 2010) were used to compile the  
 483 global crop-specific irrigation proportion data from year 1961 to 2020. Categories of cropland in HYDE  
 484 provided new distinctions with irrigated and rain-fed crops (upland crops, other than rice), irrigated and  
 485 rain-fed rice during 1960-2017. The national-level dataset of “Agricultural area actually irrigated” was  
 486 obtained from (FAO, 2022), which was used to scale the baseline year 2015 maps of irrigated area from  
 487 HYDE over the period 2016-2020. The area of irrigated upland crops from HYDE was first disaggregated

488 into 21 crops based on the irrigated proportion from MIRCA2000 for per grid cell. We assumed an even  
489 share of irrigated area by each upland crop during the period 1961-2020, like MIRCA2000. Finally, the  
490 crop-specific irrigated area was masked by reporting harvested area, then the irrigated proportion of each  
491 crop can be calculated as the crop-specific irrigated area divided by the physical area of each crop. For rice,  
492 we further divided irrigated rice into continuously and intermittently flooded systems as provided by *Cui*  
493 *et al.* (2021), and we assumed that the irrigation proportion was kept the same during the study period.  
494

## 495 **S6 Global N flow in aquaculture**

496 We applied the IMAGE-GNM aquaculture nutrient budget model for shellfish and finfish (*Bouwman et al.*,  
497 2013; *Bouwman et al.*, 2011) to calculate the nutrient flows in aquaculture production systems. These flows  
498 comprise feed inputs, retention in the fish, and nutrient excretion. Individual species within crustaceans,  
499 seaweed, fish and molluscs are aggregated to the International Standard Statistical Classification of Aquatic  
500 Animals and Plants (ISSCAAP) groups (*FAO*, 2022), for which production characteristics are specified.  
501 Feed and nutrient conversion rates are used for each ISSCAAP group to calculate the feed and nutrient  
502 intake based on production data from *FAO* (*FAO*, 2020). Feed types include home-made aquafeeds and  
503 commercial compound feeds with different feed conversion ratios that also vary in time due to efficiency  
504 improvement; in addition, the model accounts for algae in ponds, that are often fertilized with commercial  
505 fertilizers or animal manure, consumed by omnivore fish species like carp. A special case is the filter-  
506 feeding bivalves that filter seston from the water column, and excrete pseudofeces, feces and dissolved  
507 nutrients. Based on production data and tissue/shell nutrient contents, the model computes the nutrient  
508 retention in the fish. Using apparent digestibility coefficients, the model calculates outflows in the form of  
509 feces (i.e., particulate nutrients) and dissolved nutrients. Finally, nutrient deposition in pond systems and  
510 recycling are calculated. For computing the N<sub>2</sub>O emissions, we consider the amount of N released to the  
511 environment, i.e., the difference between N intake and N in the harvested fish, which includes all the  
512 nutrient excretion. Since in pond cultures part of that N is managed, we made the amount of N recycling  
513 explicit, as well as ammonia emissions from ponds. This is to avoid double counting when computing N<sub>2</sub>O  
514 emissions from crop production.  
515

## 516 **S7 Continental Shelves N<sub>2</sub>O fluxes**

517 N<sub>2</sub>O emissions from the global ocean do not include the contribution from continental shelves and are added  
518 here using the extended mask of *Laruelle et al.* (2017) to delineate the coastal ocean. This mask excludes  
519 estuaries and inland water bodies, while its outer limit is set 300 km away from the shoreline. Within this  
520 coastal ocean domain, gridded N<sub>2</sub>O emissions were calculated using one data-driven estimate and three  
521 high-resolution model estimates from two distinct models, all interpolated on the same 0.25° x 0.25° grid.  
522 Models and data are each covering different time-periods and only one climatology is provided, keeping  
523 the original timespan of each product: 1988-2017 for the observation-based product that relied on a random-  
524 forest (RF) algorithm to interpolate N<sub>2</sub>O data (*Yang et al.*, 2020) from the MEMENTO database (MEM-  
525 RF) (*Kock and Bange*, 2015), 1998-2018 for the estimate relying on the high-resolution configuration  
526 (*Berthet et al.*, 2019) of the global ocean-biogeochemical component of CNRM-ESM2-1 (CNRM-0.25°),  
527 1998-2013 and 2006-2013 for the estimates relying on the ECCO-Darwin model running at 1/3° (ECCO-  
528 Darwin1) and 1/6° (ECCO-Darwin2), respectively. The resulting climatology can be considered as broadly  
529 representative of the last 2-3 decades. Each product is further described as follows:  
530

### 531 **S7.1 MEM-RF**

532 The N<sub>2</sub>O air-sea flux reconstruction by *Yang et al.* (2020) is based on a synthesis of over 158,000  
533 observations of N<sub>2</sub>O mixing ratio, partial pressure, and concentration in the surface ocean from the  
534 MEMENTO database (<https://memento.geomar.de>) (*Kock and Bange*, 2015) and additional cruises  
535 (Dataset S1) (*Yang et al.*, 2020). N<sub>2</sub>O measurements are converted to surface N<sub>2</sub>O mixing ratio anomalies  
536 using observations from the NOAA atmospheric flask dataset (*Hall et al.*, 2007), and extrapolated to a 0.25-

537 degree resolution global monthly climatology using an ensemble of 100 random forest realizations. The  
538 random forest algorithm predicts N<sub>2</sub>O mixing ratio anomalies based on their relationship to oceanographic  
539 predictors that include hydrographic variables, nutrients, oxygen, chlorophyll, net primary production, and  
540 seafloor depth. Reconstructed mixing ratio climatologies are used to estimate air-sea fluxes by applying a  
541 commonly used gas exchange parameterization (Wanninkhof, 2014). Two formulations of piston velocity  
542 are adopted: one based on a quadratic dependence on wind speed (Wanninkhof, 2014), and one that  
543 explicitly accounts for bubble-mediated fluxes (Liang et al., 2013). Sea ice cover, surface temperature,  
544 salinity and atmospheric pressure are taken from ERA5 reanalysis (Hersbach et al., 2017). Calculations are  
545 performed with two high-resolution wind products (ERA5 and CCMP) that are available at 0.25, 6-hourly  
546 resolution for the period from 1988 to 2017, yielding four permutations of the piston velocity. The resulting  
547 ensemble of 400 global N<sub>2</sub>O air-sea flux estimates is averaged in time to obtain monthly mean climatologies.  
548 A description of the dataset and methods is presented in Yang et al. (2020). The code used to produce these  
549 datasets is archived on a public GitHub repository at <https://github.com/yangsi7/mapping-ocean-n2o> (DOI:  
550 10.5281/zenodo.3757194).

551

## 552 **S7.2 CNRM-0.25°**

553 N<sub>2</sub>O fluxes have been inferred from the global ocean-biogeochemical component of CNRM-ESM2-1  
554 (Séférian et al., 2019) run at 0.25° horizontal resolution with 75 vertical levels in the ocean. This high-  
555 resolution configuration is described in Berthet et al. (2019) and is based on the NEMOV3.6 oceanic model  
556 (Madec, 2008), the multi-category sea ice model GELATOV6 (Salas y Mélia, 2002) and the PISCESv2-gas  
557 model for marine biogeochemistry (Aumont et al., 2015), which includes an updated version of (Martinez-  
558 Rey et al., 2015) for the marine N<sub>2</sub>O module. The simulation was first spun-up during 300 years under  
559 preindustrial conditions and then has been forced by the OMIP2-compliant JRA55-do-1-5 atmospheric  
560 reanalysis (Tsuji no et al., 2020; Tsuji no et al., 2018) considering the historical evolution of CO<sub>2</sub> and N<sub>2</sub>O  
561 in the atmosphere since the year 1850. Boundary conditions for nitrogen deposition and riverine inputs are  
562 prescribed from monthly climatologies. The suboxic production of N<sub>2</sub>O uses the oxygen-dependent  
563 formulation of Jin and Gruber (2003) and is enhanced at low oxygen concentrations. This formulation  
564 encompasses N<sub>2</sub>O production during remineralization, nitrification and grazing, as well as a sink term  
565 corresponding to N<sub>2</sub>O consumption under anoxic conditions by denitrification. The oceanic N<sub>2</sub>O partial  
566 pressure is computed based on the surface N<sub>2</sub>O concentration and the N<sub>2</sub>O solubility in the ocean. Sea-to-  
567 air N<sub>2</sub>O fluxes are then computed using the standard gas exchange parameterization of Wanninkhof (1992;  
568 2014).

569

## 570 **S7.3 ECCO-Darwin & ECCO2-Darwin**

571 For this study we generated global air-sea fluxes of nitrous oxide (N<sub>2</sub>O) from the global ocean by using two  
572 models that include the same biogeochemical component but embedded in two different ocean physical  
573 settings, ECCO2-Darwin and ECCO-Darwin.

574

575 The first model, ECCO2-Darwin model, is a global physical-biogeochemical ocean model with nominal  
576 horizontal grid of 1/6 of degree therefore eddy-permitting at lower latitudes.

577 The second model is ECCO-Darwin, a global physical-biogeochemical ocean model with nominal  
578 horizontal grid resolution of 1/3 of degree (Carroll et al., 2020). The ECCO-Darwin model is forced with  
579 an atmospheric forcing corresponding to the 1992-present optimized with adjoint technique in order to  
580 realistically represent the observed physical ocean climate variability. An extensive description of this  
581 model run of ECCO2-Darwin including the optimized atmospheric forcing spanning from 2004 to 2013  
582 can be found in Manizza et al., (2019, 2023) while for ECCO-Darwin a more detailed model description  
583 can be found in Carroll et al., (2020). Both models have 50 vertical levels and in the top 100 m the model  
584 is vertically resolved with 10-meter grid boxes.

585

586 The Darwin biogeochemical/ecological model used for this study explicitly represents the cycle of carbon,  
587 oxygen, phosphorus, silica, and iron in the global ocean. It also has an ecosystem component representing  
588 five groups of phytoplankton and two groups of zooplankton (Manizza et al., 2019, Carroll et al., 2020).  
589

590 For this version of the model, we implemented a parameterization of the oceanic cycle of N<sub>2</sub>O using the  
591 scheme of Nevison et al., (2003) based on the oceanic oxygen cycle previously represented in ECCO2-  
592 Darwin model (Ganesan et al., 2020). The air-sea gas flux of N<sub>2</sub>O was parameterized according to  
593 Wanninkhof (1992).  
594

595 In the ECCO2-Darwin simulation the 2004-2005 period was discarded, and we used the 2006-2013 period  
596 only for our analysis. However, the ECCO-Darwin numerical simulation was run for the 1992-2014 period,  
597 but we discarded the inclusion of the output relative to the 1992-1996 period in our analysis due to the  
598 model adjustment in this initial part of our numerical simulation. The results of these simulations were also  
599 used in the study of Resplandy et al. (2023).  
600

## 601 **S8 Open Ocean N<sub>2</sub>O fluxes**

602 N<sub>2</sub>O is produced in the open ocean by microbial activity during organic matter cycling in the subsurface  
603 ocean, and its production pathways are influenced by the local environmental oxygen level. In the oxic  
604 ocean N<sub>2</sub>O is produced as a byproduct during the oxidation of ammonia to nitrate, mediated by ammonia  
605 oxidizing bacteria and archaea. N<sub>2</sub>O is also produced and consumed in sub-oxic and anoxic waters through  
606 the action of marine denitrifiers during the multi-step reduction of nitrate to gaseous N. The oceanic N<sub>2</sub>O  
607 distribution therefore displays significant heterogeneity with background levels of 10-20 nmol/l in the well-  
608 oxygenated ocean basins, high concentrations (> 40 nmol/l) in hypoxic waters, and N<sub>2</sub>O depletion in the  
609 core of ocean oxygen minimum zones (OMZs).  
610

611 For this synthesis open ocean N<sub>2</sub>O emissions to the atmosphere were compiled from four global ocean  
612 biogeochemistry models/Earth System models that simulate the production, consumption and circulation  
613 of oceanic N<sub>2</sub>O (Table 6). N<sub>2</sub>O flux exchange between ocean and atmosphere is derived using gas-exchange  
614 parameterizations applied to modeled surface ocean N<sub>2</sub>O. Versions of the four submitting models also  
615 participated in the previous N<sub>2</sub>O budget synthesis (Tian et al., 2020a). Model details and updates to the  
616 previous N<sub>2</sub>O budget synthesis are summarized below.

617 The models differ in aspects of physical configuration (e.g., spatial resolution), meteorological forcing  
618 applied at the ocean surface, and in their parameterizations of ocean biogeochemistry; specific details on  
619 individual models are provided in the publications listed in Table 1. Towards this N<sub>2</sub>O budget synthesis,  
620 modelling groups reported grid-resolved (1°×1° horizontal resolution) monthly estimates of ocean-  
621 atmosphere N<sub>2</sub>O fluxes for the period 1980-2020 (or for as many years as possible in that period).  
622

### 623 **S8.1 U. Bern: Bern-3D**

624 N<sub>2</sub>O fluxes are derived from the Bern-3D Earth System Model of Intermediate Complexity which includes  
625 a prognostic marine biogeochemistry model (based on (Parekh et al., 2008) and (Tschumi et al., 2011)).  
626 Configuration of the model for simulation of N<sub>2</sub>O is outlined in Battaglia and Joos (2018). Model  
627 simulations were run at a native resolution of horizontal resolution of 41 by 40 grid cells and 32  
628 logarithmically scaled vertical layers. Modifications of the biogeochemistry model relevant for the N<sub>2</sub>O  
629 cycle include the assignment of organic matter remineralization to aerobic and anaerobic pathways  
630 dependent on mean grid-cell dissolved oxygen level. N<sub>2</sub>O is produced by nitrification as a product of  
631 remineralization rate and a specified N<sub>2</sub>O yield which has a functional form dependent on oxygen level (see  
632 details in (Battaglia and Joos, 2018)). N<sub>2</sub>O consumption by denitrification processes is represented by a  
633 first-order kinetics formulation which also includes a dependence on local oxygen level to account for the  
634 relative importance of denitrification-related N<sub>2</sub>O production and consumption processes in each gridcell.  
635 Measurements of dissolved N<sub>2</sub>O (surface and interior) from the MEMENTO database (Kock and Bange,



636 2015) together with an ensemble of model runs are used to constrain the model parameters governing N<sub>2</sub>O  
637 production and consumption mechanisms. From a pre-industrial equilibrium state the model is forced by  
638 historical CO<sub>2</sub> emissions, non-CO<sub>2</sub> radiative forcing, and land-use changes. N<sub>2</sub>O in the atmosphere is  
639 prescribed based on historical data.

640  
641

### **S8.2 CNRM: CNRM-ESM2-1**

642 N<sub>2</sub>O fluxes are provided by the CNRM-ESM2-1 Earth System model. The ocean model component is based  
643 on NEMO Version 3.6 (*Madec et al.*, 2017) and coupled to the GELATO sea ice model (*Salas y Mélia,*  
644 2002) Version 6 and the marine biogeochemical model PISCESv2-gas (*Aumont et al.*, 2015). The spatial  
645 model resolution follows the eORCA1L75 grid, with a nominal horizontal resolution of 1° and with higher  
646 resolution in the tropics (increasing to  $\sim(1/3)^\circ$ ). The model has 75 vertical levels with higher resolution  
647 towards the ocean surface. The simulations were forced at the surface by the atmospheric state of JRA55-  
648 do v1.5.0 (*Tsujino et al.*, 2018). Atmospheric N<sub>2</sub>O concentration is given as annual means as specified by  
649 CMIP6 protocols and is linearly interpolated in time. Parameterization of the marine N<sub>2</sub>O cycle follows that  
650 of *Martinez-Rey et al.* (2015) with some modifications. N<sub>2</sub>O production is driven by an oxygen-dependent  
651 yield of N<sub>2</sub>O, which encompasses production from denitrification and nitrification processes. This  
652 formulation also assumes a constant background yield representing N<sub>2</sub>O production by nitrification and a  
653 consumption of N<sub>2</sub>O in suboxic conditions. Originally implemented by *Martinez-Rey et al.* (2015), the  
654 marine N<sub>2</sub>O parameterization has benefited from a recoding and an improved calibration presented in  
655 *Berthet et al.* (2023). Further details of the model biogeochemistry and configuration are provided by  
656 *Séférian et al.* (2019) and *Berthet et al.* (2019).

657  
658

### **S8.3 UVic2.9**

659 N<sub>2</sub>O model fluxes are derived from the UVic2.9, Earth System Model of Intermediate Complexity with  
660 prescribed monthly climatological winds (*Kalnay et al.*, 1996) and ice sheets (*Peltier*, 2004), configuration  
661 outlined in *Landolfi et al.* (2017). Oceanic subsurface N<sub>2</sub>O production is parameterized following (*Zamora*  
662 *and Oschlies*, 2014), as a function of O<sub>2</sub> consumption with a linear O<sub>2</sub> dependency, inherently including  
663 both nitrification and denitrification. In O<sub>2</sub>-deficient waters ( $<4 \text{ mmol m}^{-3}$ ), denitrification becomes a sink  
664 of N<sub>2</sub>O consumed at a constant rate. The gradient driving the air-sea N<sub>2</sub>O gas exchange, is computed online  
665 based on departure of the surface ocean concentration from the saturation value using the solubility  
666 coefficients of *Weiss and Price* (1980) and time-varying prescribed atmospheric N<sub>2</sub>O concentrations  
667 (historical and RCP8.5). The model was spun-up for 6000 years with preindustrial boundary conditions  
668 (solar and volcanic and aerosol forcing, fixed atmospheric CO<sub>2</sub> of 280 ppm and N<sub>2</sub>O of 276 ppb, and  
669 preindustrial atmospheric N deposition).

670

### **S8.4 UEA: NEMO-PlankTOM10.2**

672 N<sub>2</sub>O model fluxes are derived from the NEMO-PlankTOM10.2 ocean model. The physical circulation  
673 component is NEMO v3.1 (*Madec*, 2008), with horizontal resolution of 2° longitude, and a variable  
674 latitudinal resolution (average  $\sim 1^\circ$ ) with higher resolution in the tropics and polar regions. The model has  
675 30 vertical layers, with variable resolution ranging from 10m in the upper 100m to 500m at depths of 5000  
676 m. The biogeochemical component relies on the marine ecosystem model PlankTOM10, which includes  
677 representation of 10 plankton functional types (*Le Quéré et al.*, 2016). It has been extended by *Buitenhuis*  
678 *et al.* (2018) to include nitrogen cycle processes, and prognostic and diagnostic models of N<sub>2</sub>O production.  
679 N<sub>2</sub>O is produced from nitrification and denitrification pathways, with oxygen dependent yields employed  
680 to account for varying production and consumption processes in hypoxic waters. Nitrogen cycle parameters  
681 are optimized using ocean databases of dissolved N<sub>2</sub>O (MEMENTO, *Kock and Bange* (2015)) nitrification  
682 rates (*Yool et al.*, 2007), and surface ammonium concentrations (*Johnson et al.*, 2015; *Paulot et al.*, 2015).  
683 Further details on model configuration are provided in (*Buitenhuis et al.*, 2018).

684

## 685 **S9 Net N<sub>2</sub>O emission from land cover change**

686 This section mainly involves the calculation of post-deforestation N<sub>2</sub>O emissions, deforestation induced  
687 N<sub>2</sub>O reduction and N<sub>2</sub>O emissions from forest regrowth (afforestation or reforestation). The methods  
688 include both bookkeeping and process-based modeling.

689

### 690 **S9.1 Deforestation area, crop/pasture expansion and secondary forests**

691 The LUH2 v2h (land use harmonization, <http://luh.umd.edu>) land use data was used to derive the  
692 deforestation area and its partition between crops and pastures during 1860–2020. LUH2 categorizes forest  
693 lands into forested primary land and potentially forested secondary land, while croplands are divided into  
694 C3 annual crops, C3 perennial crops, C4 annual crops, C4 perennial crops, and C3 N-fixing crops.

695

696 In the empirical computation of deforestation induced N<sub>2</sub>O emissions, all sub-classes within each land use  
697 type were treated the same. Thus, only the annual transition area from forests to croplands or managed  
698 pasture was needed. In the process-based estimates, the DLEM model was improved to further account for  
699 the classifications of primary forests, secondary forests (further partitioned into established and newly  
700 converted by an age threshold of 15 years), croplands/pastures /rangelands (further partitioned into  
701 established and newly converted by an age threshold of seven nine years). Each land use type can be divided  
702 into several different plant functional types (PFTs). Specifically, within a grid cell, cropland can only be  
703 dominated by only one crop type. The pastures and rangelands can be either C3 type or C4 type. To generate  
704 the historical spatial distribution of PFTs, a potential vegetation map and the accompanied composition  
705 ratio map of each natural PFT acquired from the Synergetic Land Cover Product (SYNMAP) were jointly  
706 used with LUH2 v2h.

707

### 708 **S9.2 Methods**

709 The bookkeeping method was mainly applied to the tropical areas, where forests generally have high N<sub>2</sub>O  
710 emissions. Specifically, the average tropical forest N<sub>2</sub>O emission rate of 1.974 kg N<sub>2</sub>O-N ha<sup>-1</sup> yr<sup>-1</sup> was  
711 adopted as the baseline. Two logarithmic response curves of soil N<sub>2</sub>O emissions (normalized to the baseline)  
712 after deforestation were developed:  $y = -0.31 \ln(x) + 1.53$  and  $y = -0.454 \ln(x) + 2.21$ . This form of  
713 the response functions can effectively reproduce the short-lived increase in soil N<sub>2</sub>O emissions after initial  
714 forest clearing and the gradually declining emission rates of converted crops/pastures (*Melillo et al.*, 2001;  
715 *Verchot et al.*, 1999). Using these two curves and the baseline, we kept track of the N<sub>2</sub>O reduction of tropical  
716 forests and the post-deforestation crop/pasture N<sub>2</sub>O emissions at an annual timescale.

717

718 There are not many studies on N<sub>2</sub>O emissions from secondary tropical forests that regrowth after crop or  
719 pasture abandonment. *Sullivan et al.* (2019) lumped together all forms of N "gas loss" including NO and  
720 N<sub>2</sub>O for secondary forests across the tropics and the results showed gas loss gradually increases with age  
721 since the regrowth of secondary forest. *Keller and Reiners* (1994) also reported a gradual recovery of soil  
722 nitrate and soil emissions of N<sub>2</sub>O and nitric oxide (NO) during 20 years of secondary forest succession,  
723 which however did not return to the level of the primary forests. In this study, using field observations from  
724 *Davidson et al.* (2007) and *Keller and Reiners* (1994), we regressed normalized N<sub>2</sub>O emissions (relative to  
725 a reference mature forest) of secondary tropical forests with their ages as  $y = 0.0084x + 0.2401$  ( $R^2 = 0.44$ ;  
726 unit of  $x$  is year). The derived  $y$  values were multiplied by tropical forest N<sub>2</sub>O emissions estimated by  
727 NMIP2 models that do not distinguish secondary forests from primary forests.

728

729 The DLEM model was run with varying climate and CO<sub>2</sub> with other factors held constant to estimate forest  
730 baseline emissions and unfertilized crop/pasture emissions from 1860-2020. The climate data were acquired  
731 from CRUJRA, which is a fusion of the CRU and JRA reanalysis products at a spatial resolution of 0.5° ×  
732 0.5° and a daily time-step. The atmospheric CO<sub>2</sub> data were obtained from NOAA GLOBLVIEW-CO2  
733 dataset (<https://www.esrl.noaa.gov>), which are derived from atmospheric and ice core measurements. In

734 the tropical area, both estimates from the DLEM model and the bookkeeping method were adopted, whereas  
735 in extra-tropical area, we only adopted the DLEM outputs.

736

## 737 **S10 Inland water, estuaries, and coastal vegetation**

738

### 739 **S10.1 Dynamic Land Ecosystem Model-Terrestrial/Aquatic Continuum (DLEM-TAC)**

740 To quantify N<sub>2</sub>O emissions from global inland waters (rivers, lakes, and reservoirs), we use a process-based  
741 coupled terrestrial-aquatic model, which builds up on the Dynamic Land Ecosystem Model (DLEM).  
742 DLEM-TAC is a fully distributed, process-based land surface model which couples the major land  
743 processes (terrestrial hydrology, plant phenology and physiology, soil biogeochemistry) and aquatic  
744 dynamics (lateral transport and in-stream biogeochemistry) (Pan *et al.*, 2021; Tian *et al.*, 2015; Tian *et al.*,  
745 2020b; Yao *et al.*, 2020). The land component of DLEM-TAC explicitly simulates the carbon, nitrogen,  
746 and water fluxes between plants, soil, and atmosphere, and the surface and drainage runoff and nitrogen  
747 load from the land module are used as input for the aquatic module. The simulated nitrogen load  
748 includes dissolved inorganic nitrogen (DIN), dissolved organic nitrogen (DON), particulate organic  
749 nitrogen (PON), and runoffs, sewers as the initial condition of the aquatic module.

750

751 DLEM-TAC aquatic module calculated lateral water transport and the associated aquatic biogeochemical  
752 processes by adopting a scale-adaptive scheme. The water transport scheme, which coupled hillslope flow,  
753 subnetwork flow, and main channel flow, simulated the water transport processes within grid cells. In the  
754 aquatic module, lakes and reservoirs were linked with small streams and large rivers, forming a river-lake-  
755 reservoir corridor (Wollheim *et al.*, 2008)). Particularly, lakes that are linked to small streams are typically  
756 small in size and are defined as small lakes, while those linked to large rivers are usually had large size and  
757 are defined as large lakes; similarly, reservoirs that are linked to main channels are considered as large  
758 reservoirs, while those that are linked to small streams are considered as small reservoirs. The incoming  
759 flow of a linked river-lake-reservoir corridor drains to lakes first, and the outflow rate of lakes and reservoirs  
760 is determined based on the predefined residence time obtained from the global lake dataset (Lehner *et al.*,  
761 2011; Messenger *et al.*, 2016; Yao *et al.*, 2022). The aquatic N module was developed based on the scale  
762 adaptive water transport scheme, including lateral transport, decomposition of organic matter, particle  
763 organic matter deposition, nitrification, and denitrification. The detailed description could be found in the  
764 previous studies (Pan *et al.*, 2021; Tian *et al.*, 2020b; Yao *et al.*, 2020).

765

766 Following our previous work referring to the development of water transport and biogeochemistry, we  
767 developed an inland water N<sub>2</sub>O module within the aquatic biogeochemical component of the DLEM  
768 framework (Yao *et al.*, 2020). The net fluxes of dissolved N<sub>2</sub>O (including physical and biogeochemical  
769 processes) in the main channel (high-order streams) and subnetwork (small rivers) are estimated as:

770

$$(ΔM_{N_2O}) / Δt = Fa + Y_{water} + D - R - E \quad (26)$$

771 where M<sub>N<sub>2</sub>O</sub> is the total mass of dissolved N<sub>2</sub>O in the main channel or subnetworks (g N), Δt is the time  
772 step, Fa is advective N<sub>2</sub>O fluxes (g N d<sup>-1</sup>), Y<sub>water</sub> is the N<sub>2</sub>O production within the water column (g N d<sup>-1</sup>),  
773 D is the dissolved N<sub>2</sub>O from rainfall to rivers (i.e. deposition) (g N d<sup>-1</sup>) with an initial concentration equal  
774 to the atmospheric equilibrium N<sub>2</sub>O concentration, R is the flux from N<sub>2</sub>O reduction (g N d<sup>-1</sup>) to nitrogen  
775 gas, and E is the riverine N<sub>2</sub>O efflux (g N d<sup>-1</sup>) through the air-water interface.

776

777 Input data. The driving data of DLEM-TAC include the climate variables, atmospheric CO<sub>2</sub> concentration,  
778 land use change, nitrogen (N) deposition, N fertilizer, and manure application with a spatial resolution of  
779 0.5° × 0.5°. The daily climate variables (precipitation, mean temperature, maximum temperature, minimum  
780 temperature, and shortwave radiation) were obtained from the CRUNCEP dataset (<https://vesg.ipsl.upmc.fr>)

781 for 1901-2019. Climate data of each year during 1850-1900 was randomly sampled from 1901-1920.  
782 Annual atmospheric CO<sub>2</sub> concentration from 1900-2019 was obtained from the NOAA GLOBALVIEW-  
783 CO<sub>2</sub> dataset (<https://www.esrl.noaa.gov>). The annual land use change data was derived from a potential  
784 natural vegetation map (synergetic land cover product) and a prescribed cropland area dataset from the  
785 history database of the global environment v.3.2 (HYDE 3.2, <ftp://ftp.pbl.nl/hyde>). The data of N fertilizer,  
786 manure N application, and N deposition data was obtained from (*Tian et al.*, 2022).  
787

788 In the aquatic module, the required channel dataset included channel slope, channel width, and channel  
789 length generated from the Hydrosched dataset (*Lehner et al.*, 2008) and DDM30 dataset (*Döll and Lehner*,  
790 2002). The flow direction and distance data were obtained from the Dominant River Tracing (DRT) dataset.  
791 For modeling water dynamics in lakes and reservoirs, we generated 0.5 grid level surface water area,  
792 upstream area, volume, depth, and average residence time for lakes based on the Hydrolakes dataset  
793 (*Messenger et al.*, 2016), while the GRanD database provided the same information for reservoirs (*Lehner*  
794 *et al.*, 2011).  
795

796 Simulation protocol. DLEM-TAC simulations include three steps: equilibrium run, spin-up run and two  
797 transit runs, one with dam operation close, and another one with dam operation open. First, the equilibrium  
798 run is required to obtain the initial and steady condition of carbon, nitrogen, and water pool at the pre-  
799 industrial level in each grid cell (*Thornton and Rosenbloom*, 2005). In this step, we held all the driving  
800 forces such as climate data, atmospheric CO<sub>2</sub> concentration, land use data, and nitrogen additions consistent  
801 with the first year's data we used in the simulation. Second, we conducted a 30-year spin-up run by  
802 randomly selecting climate data within the 1850s (*Tian et al.*, 2012a). This step can alleviate the disturbance  
803 of driving data changes in the transit run. Then we conduct the natural flow simulation with the dam model  
804 temporarily closed, and all the driving forces change over time. After the natural flow simulation, we set  
805 up a management flow simulation with the dam module open, specifically the dam module needs natural  
806 flow in the previous run as model input.  
807

## 808 **S10.2 Mechanistic Stochastic Modeling of N<sub>2</sub>O emissions from large rivers, lakes, reservoirs, and** 809 **estuaries:**

810  
811 To calculate the cascading loads of TN and TP delivered to each water body along the river-reservoir-  
812 estuary continuum, we spatially routed all reservoirs from the GRanD database (*Lehner et al.*, 2011), with  
813 river networks from Hydroscheds 15s (*Lehner et al.*, 2008) and, at latitudes above 50°N, Hydro1K  
814 (<http://edc.usgs.gov/products/elevation/gtopo30/hydro/>), which were in turn connected to estuaries as  
815 represented in the “Worldwide Typology of Nearshore Coastal Systems” of *Dürr et al.* (2011). In addition,  
816 the global database HydroLAKES (*Messenger et al.*, 2016) was used to topologically connect 1.4 million  
817 lakes with a minimum surface area of 0.1 km<sup>2</sup> within the river network. Note that besides natural lakes,  
818 HydroLAKES includes updated information on 6,796 reservoirs from the GRanD database, which was used  
819 in the study of *Maavara et al.* (2019). In order to estimate the TN and TP loads to each water body, we then  
820 relied on a spatially explicit representation of TN and TP mobilization from the watershed into the river  
821 network (see (*Maavara et al.*, 2019) for details (*Bouwman et al.*, 2009; *Van Drecht et al.*, 2009)).  
822

823 For the estimation of N<sub>2</sub>O emission, we applied two distinct model configurations, respectively named DS1  
824 and DS2 in *Maavara et al.* (2019). DS1 estimates N<sub>2</sub>O emissions from denitrification and nitrification based  
825 on an EF of 0.9%, which is in the mean of published values (*Beaulieu et al.*, 2011), and the assumption that  
826 N<sub>2</sub>O production equals N<sub>2</sub>O emissions (*Maavara et al.*, 2019). For DS2, the reduction of N<sub>2</sub>O to N<sub>2</sub> during  
827 denitrification if N<sub>2</sub>O is not evading sufficiently rapidly from the water body is considered. The fluxes in  
828 the model represent lumped sediment-water column rates and were resolved at the annual timescale. The  
829 use of water residence time as an independent variable in both the mechanistic model and the upscaling  
830 process introduces an important kinetic refinement to existing global N<sub>2</sub>O emission estimates. Rather than

831 applying an average EF (directly scaling N<sub>2</sub>O emissions to N inputs) to all water bodies, the use of water  
832 residence time explicitly adjusts for the extent of N<sub>2</sub>O production and emission that is kinetically possible  
833 within the timeframe available in a given water body. Simulated N<sub>2</sub>O emission rates were evaluated against  
834 UNFCCC measurement-based upscaling methods applied to reservoirs (*Deemer et al.*, 2016) and rivers  
835 (*Hu et al.*, 2016) as well as a UNFCCC observation-driven regional estimate of lake N<sub>2</sub>O emissions based  
836 on literature data (*Lauerwald et al.*, 2019).

837

### 838 **S10.3 Meta analysis-based N<sub>2</sub>O emissions from large rivers**

839 Data from 70 published studies between 1998 and 2016 that provided N<sub>2</sub>O emission from streams and rivers  
840 were compiled by *Hu et al.* (2016). The N<sub>2</sub>O emission factors (EF = N<sub>2</sub>O /DIN) and emission rates (ER =  
841 EF \* DIN load, kg N<sub>2</sub>O-N yr<sup>-1</sup>) were calculated for each studied river. Exploratory multiple regression  
842 analyses were conducted to predict EF and ER using various combinations of factors (N concentrations,  
843 loads, yields, DOC: DIN, discharge, and watershed area) and different functions. Among them, DIN yield  
844 (kg N yr<sup>-1</sup> km<sup>-2</sup>) was identified as the best predictor of EF and ER. Using the optimal model and DIN loads  
845 for 6400 global rivers calculated by the NEWS2-DIN-S model (*McCrackin et al.*, 2014), we estimated  
846 global riverine N<sub>2</sub>O emissions (*Hu et al.*, 2016).

847

### 848 **S10.4 Stream and river N<sub>2</sub>O emissions combining machine-learning and model-based upscaling**

849 *Marzadri et al.* (2021) developed a novel approach that combines a data-driven Random Forest Machine  
850 Learning (RM-ML) model with a physically-based upscaling model to predict near global (neglecting  
851 Arctic and Antarctic areas) riverine N<sub>2</sub>O emissions flux (F\*N<sub>2</sub>O given by the ratio between the flux of N<sub>2</sub>O,  
852 FN<sub>2</sub>O, and the in-stream flux of dissolved inorganic nitrogen species FDIN) from both surface (i.e. water  
853 column) and subsurface (i.e. benthic zone and hyporheic zone) riverine environments. In particular, to  
854 capture the local scale processes responsible for N<sub>2</sub>O emissions and to provide estimations at different  
855 spatial scales (from local reach up to the global scale) the model compute two different denitrification  
856 Damköhler numbers (given by the ratio between a characteristics time of transport and a characteristics  
857 time of denitrification (*Marzadri et al.*, 2021; *Marzadri et al.*, 2017)) starting from the hydro-morphological  
858 and biogeochemical information provided by the RM-ML model. Model results at the local reach scale  
859 shows that nearly 50% of the riverine N<sub>2</sub>O emissions comes from small streams (i.e. widths lower than 10  
860 m, although they represent only the 13% of the total riverine surface area worldwide) while at the large  
861 scale predict a near-global annual riverine N<sub>2</sub>O emissions around 72.8 GgN<sub>2</sub>O – N/yr.

862

### 863 **S10.5 Meta-analysis based N<sub>2</sub>O emissions from estuaries and coastal vegetation**

864 N<sub>2</sub>O emissions from estuaries and coastal vegetated ecosystems were obtained from a meta-analysis of  
865 observed N<sub>2</sub>O fluxes (*Rosentreter et al.*, 2023). In brief, the meta-data analysis relies on a categorization of  
866 estuaries into ‘tidal systems and deltas’, ‘lagoons’, and ‘fjords’. Water-air N<sub>2</sub>O fluxes from 123 estuary  
867 sites globally were then compiled from peer-reviewed publications until the end of 2020. Coastal vegetation  
868 comprises ‘mangrove’, ‘salt marsh’, and ‘seagrass’ ecosystems and N<sub>2</sub>O sediment-water-air fluxes were  
869 compiled from 55 sites globally from peer-reviewed publications until the end of 2020. A non-parametric  
870 bootstrapping method (1000 iterations of the median of samples) was used to resample N<sub>2</sub>O fluxes per unit  
871 area for each estuary and coastal vegetation type in each of the 18 regions using the ‘boot’ function in the  
872 package ‘boot’ in R software. Results from the bootstrapping output (minimum, Q1, median, mean, Q3,  
873 maximum) were then scaled to the surface area of each estuary and coastal vegetation type in each of the  
874 18 regions. If an ecosystem type had less than three sites in a region, we applied the global statistics of this  
875 type in this region. Note that the meta-data analysis only provides flux assessments at the scale of the 18  
876 regions.

877

### 878 **S11 Atmospheric inversion models**

879 Emissions were estimated using four independent atmospheric inversion frameworks (see Table 1). The  
 880 frameworks all used a Bayesian inversion method. The approach used here finds the maximum posteriori  
 881 (MAP), or optimal, estimate of emissions, that is, those, which when coupled to a model of atmospheric  
 882 transport, provide the best agreement to observed N<sub>2</sub>O mixing ratios while being guided by their prior  
 883 probability. In this particular case, where both the likelihood and prior probability are assumed to be  
 884 distributed normally, the optimal emissions are equivalent to those that minimize the cost function,  
 885

$$886 \quad J(\mathbf{x}) = \frac{1}{2}(\mathbf{x} - \mathbf{x}_b)^T \mathbf{B}^{-1}(\mathbf{x} - \mathbf{x}_b) + \frac{1}{2}(\mathbf{y} - H(\mathbf{x}))^T \mathbf{R}^{-1}(\mathbf{y} - H(\mathbf{x})) \quad (27)$$

887  
 888 where  $\mathbf{x}$  and  $\mathbf{x}_b$  are, respectively, vectors of the multivariate means of the posterior and prior emission  
 889 distributions,  $\mathbf{B}$  is the prior error covariance matrix for emissions,  $\mathbf{y}$  is a vector of observed N<sub>2</sub>O mixing  
 890 ratios,  $\mathbf{R}$  is the observation error covariance matrix, and  $H(\mathbf{x})$  is the model of atmospheric transport (for  
 891 details on the inversion method see (*Tarantola, 2005*)). The optimal emissions,  $\mathbf{x}$ , were found by solving  
 892 the first order derivative of equation (21):  
 893

$$894 \quad J'(\mathbf{x}) = \mathbf{B}^{-1}(\mathbf{x} - \mathbf{x}_b) + (H'(\mathbf{x}))^T \mathbf{R}^{-1}(\mathbf{y} - H(\mathbf{x})) = 0 \quad (28)$$

895  
 896 where  $(H'(\mathbf{x}))^T$  is the sensitivity of the atmospheric observations to emissions, derived from an adjoint  
 897 model of transport. In frameworks INVICAT, PyVAR-CAMS and GEOS-Chem, equation (5b) was solved  
 898 using a variational approach (*Thompson et al., 2014; Wells et al., 2015; Wilson et al., 2014*), which uses a  
 899 descent algorithm and computations involving the forward and adjoint models. In framework MIROC4-  
 900 ACTM (*Patra et al., 2018*), equation (22) was solved directly by computing a transport operator,  $\mathbf{H}$  from  
 901 integrations of the forward model, such that  $\mathbf{H}\mathbf{x}$  is equivalent to  $H(\mathbf{x})$ , and taking the transpose of  $\mathbf{H}$  (*Patra*  
 902 *et al., 2022*).  
 903

904 Each of the inversion frameworks used a different model of atmospheric transport with different horizontal  
 905 and vertical resolutions (see Table 1). The transport models TOMCAT and LMDz5, used in INVICAT and  
 906 PyVAR-CAMS respectively, were driven by ECMWF ERA-5 and ERA-Interim wind fields respectively,  
 907 MIROC4-ACTM was driven by JRA-55 wind fields, and GEOS-Chem was driven by MERRA-2 wind  
 908 fields. While INVICAT, PyVAR-CAMS, and GEOS-Chem optimized the emissions at the spatial  
 909 resolution of the transport model, MIROC4-ACTM optimized the error in the emissions aggregated into 84  
 910 land and ocean regions. All frameworks optimized the emissions with monthly temporal resolution. The  
 911 transport models included an online calculation of the loss of N<sub>2</sub>O in the stratosphere due to photolysis and  
 912 oxidation by O(<sup>1</sup>D) resulting in mean atmospheric lifetimes of between 118 and 129 years, broadly  
 913 consistent with recent independent estimates of the lifetime of 116±9 yr (*Prather et al., 2015*).  
 914

915 All inversions used N<sub>2</sub>O measurements of discrete air samples from the National Oceanic and Atmospheric  
 916 Administration Carbon Cycle Cooperative Global Air Sampling Network (NOAA). In addition, discrete  
 917 measurements from the Commonwealth Scientific and Industrial Research Organisation network (CSIRO)  
 918 as well as in-situ measurements from the Advanced Global Atmospheric Gases Experiment network  
 919 (AGAGE), the NOAA CATS network, and from individual sites operated by University of Edinburgh (UE),  
 920 National Institute for Environmental Studies (NIES), the Finnish Meteorological Institute (FMI) and the  
 921 Japan Meteorological Agency (JMA) were included in INVICAT, PyVAR-CAMS and GEOS-Chem.  
 922 Measurements from networks other than NOAA were corrected to the NOAA calibration scale, NOAA-  
 923 2006A, using the results of the WMO Round Robin inter-comparison experiment  
 924 (<https://www.esrl.noaa.gov/gmd/ccgg/wmorr/>), where available. For AGAGE and CSIRO, which did not  
 925 participate in the WMO Round Robins, the data at sites where NOAA discrete samples are also collected  
 926 were used to calculate a linear regression with NOAA data, which was applied to adjust the data to the

927 NOAA-2006A scale. For the remaining CSIRO sites where there were no NOAA discrete samples, the  
928 mean regression coefficient and offset from all other CSIRO sites were used. The inversions used the  
929 discrete sample measurements without averaging, and hourly or daily means of the in-situ measurements,  
930 depending on the particular inversion framework.

931  
932 Each framework applied its own method for calculating the observation space uncertainty, the square of  
933 which gives the diagonal elements of the observation error covariance matrix  $R$ . The observation space  
934 uncertainty accounts for measurement and model representation errors and is equal to the quadratic sum of  
935 these terms. Typical values for the observation space uncertainty were between 0.3 and 0.5 ppb for all  
936 inversion frameworks.

937  
938 Prior mean emissions were based on estimates from terrestrial biosphere and ocean biogeochemistry models  
939 as well as from inventories. INVICAT, PyVAR-CAMS and GEOS-Chem used the same prior estimates for  
940 emissions from natural and agricultural soils from the model OCN v1.1 (Zaehle *et al.*, 2011) and for biomass  
941 burning emissions from GFEDv4.1s. For non-soil anthropogenic emissions (namely those from energy,  
942 industry and waste sectors), INVICAT, PyVAR-CAMS, and GEOS-Chem used EDGAR v5. MIROC4-  
943 ACTM used the VISIT model (Inatomi *et al.*, 2010; Ito *et al.*, 2018) for emissions from natural soils and  
944 EDGAR 4.2 for all anthropogenic emissions, including agricultural waste burning, but did not explicitly  
945 include a prior estimate for wildfire emissions.

946  
947 For the prior mean estimate of ocean fluxes, INVICAT, PyVAR-CAMS and GEOS-Chem used the  
948 prognostic version of the PlankTOM-v10.2 model (Buitenhuis *et al.*, 2018) with a global total source 2.5  
949 TgN yr<sup>-1</sup>. Prior uncertainties were estimated in all the inversion frameworks for each grid cell (INVICAT,  
950 PyVAR-CAMS and GEOS-Chem) or for each region (MIROC4-ACTM) and the square of these  
951 uncertainties formed the diagonal elements of the prior error covariance matrix  $B$ . INVICAT, PyVAR-  
952 CAMS and GEOS-Chem estimated the uncertainty as proportional to the prior value in each grid cell, but  
953 MIROC4-ACTM set the uncertainty uniformly for land regions at 1 Tg N yr<sup>-1</sup> and for ocean regions at 0.5  
954 Tg N yr<sup>-1</sup>. INVICAT also included off-diagonal covariances in  $B$  corresponding to a spatial correlation  
955 between flux uncertainties of 500 km and assumed a semi-exponential distribution of uncertainties so as to  
956 restrict the possibility of negative fluxes.

957

958

## 959 **S12 Atmospheric N<sub>2</sub>O Observation Networks**

960

### 961 **S12.1 The NOAA Network:**

962 For atmospheric N<sub>2</sub>O observations from the NOAA network (Dutton *et al.* 2023), we used global mean  
963 mixing ratios from the NOAA Global Monitoring Laboratory (GML) (combined dataset based on  
964 measurements from five different measurement programs [HATS old flask instrument, HATS current flask  
965 instrument (OTTO), the Carbon Cycle and Greenhouse Gases (CCGG) group Cooperative Global Air  
966 Sampling Network (<https://www.esrl.noaa.gov/gmd/ccgg/flask.php>), HATS in situ (RITS program), and  
967 HATS in situ (CATS program)]. CCGG provides uncertainties with each measurement (see site files:  
968 [ftp://aftp.cmdl.noaa.gov/data/greenhouse\\_gases/n2o/flask/surface/](ftp://aftp.cmdl.noaa.gov/data/greenhouse_gases/n2o/flask/surface/)). The CCGG measurements for N<sub>2</sub>O  
969 analysis from more than 50 sites globally was changed to tunable infrared laser direct absorption  
970 spectroscopy (TILDAS) in mid-2019 from gas chromatography. About 40 sites of them (mostly Marine  
971 Boundary Layer sites) are used to calculate CCGG monthly mean global N<sub>2</sub>O levels. Monthly mean  
972 observations from different NOAA measurement programs are statistically combined to create a long-term  
973 NOAA/ESRL GML dataset. Uncertainties (1 sigma) associated with monthly estimates of global mean  
974 N<sub>2</sub>O, are ~1 ppb from 1977–1987, 0.6 ppb from 1988–1994, 0.3–0.4 ppb from 1995–2000, and 0.1 ppb  
975 from 2001–2017. NOAA data are generally more consistent after 1995, with standard deviations on the  
976 monthly mean mixing ratios at individual sites of ~0.5 ppb from 1995–1998, and 0.1–0.4 ppb after 1998.

977 A detailed description of these measurement programs and the method to combine them are available via  
 978 <https://www.esrl.noaa.gov/gmd/hats/combined/N2O.html>.

979  
 980 **S12.2 The AGAGE network:**  
 981 The Advanced Global Atmospheric Gases Experiment (AGAGE) global network (and its predecessors ALE  
 982 and GAGE) (Prinn et al., 2018) has made continuous high-frequency gas chromatographic (GC)  
 983 measurements with electronic capture detection (ECD) of N<sub>2</sub>O at five globally distributed sites since 1978.  
 984 Improved GC/ECD methods have been deployed over time resulting in N<sub>2</sub>O measurement precision of  
 985 about 0.35% in ALE, 0.13% in GAGE (Prinn et al., 1990) and 0.05% in AGAGE (Prinn et al., 2008; 2018).  
 986 We used the global mean of AGAGE N<sub>2</sub>O measurements during 1980–2020 which are reported on the  
 987 Scripps Institution of Oceanography SIO-16 scale. Further information on AGAGE stations, instruments,  
 988 calibration, uncertainties and access to data is available at the AGAGE Data website:  
 989 <https://www.osti.gov/dataexplorer/biblio/dataset/1841748>.

990  
 991 **S12.3 The CSIRO network:**  
 992 The CSIRO flask network (Francey et al., 2003) consists of nine sampling sites distributed globally and has  
 993 been in operation since 1992. Flask samples are collected approximately every two weeks and shipped back  
 994 to CSIRO GASLAB for analysis. Samples were analyzed by gas chromatography with electron capture  
 995 detection (GC-ECD). One Shimadzu gas chromatograph labelled “Shimadzu-1” (S1) has been used over  
 996 the entire length of the record and the measurement precision for N<sub>2</sub>O from this instrument is about 0.1%.  
 997 N<sub>2</sub>O data from the CSIRO global flask network are reported on the NOAA-2006A N<sub>2</sub>O scale and are  
 998 archived at the World Data Centre for Greenhouse Gases (WDCGG: <https://gaw.kishou.go.jp/>). Nine sites  
 999 from the CSIRO network were used to calculate the annual global N<sub>2</sub>O mole fractions. Smooth curve fits  
 1000 to the N<sub>2</sub>O data from each of these sites were calculated using the technique outlined in Thoning et al.  
 1001 (1989), using a short-term cut-off of 80 days. The smooth curve fit data were then placed on an evenly  
 1002 spaced latitude (5 degree) versus time (weekly) grid using the Kriging interpolation technique. Finally, the  
 1003 gridded data were used to calculate the global annual values.

1004  
 1005 **Table S3 Factors used to convert N<sub>2</sub>O in various units (by convention Unit 1=Unit 2 × conversion)**

Unit 1	Unit 2	Conversion
Tg N <sub>2</sub> O (teragrams of N <sub>2</sub> O)	Tg N (teragrams of nitrogen)	1.57
Tg N (teragrams of nitrogen)	g N (grams of nitrogen)	10 <sup>-12</sup>
Tg N (teragrams of nitrogen)	ppb (parts per billion)	4.79

1006  
 1007 **Table S4 Atmospheric N<sub>2</sub>O dry mole fraction measured by different observing networks during 2000-**  
 1008 **2022.**

ppb	NOAA	AGAGE	CSIRO	Min	Max
2000	315.58	316.18	315.48	315.48	316.18
2001	316.33	316.95	316.12	316.12	316.95
2002	316.99	317.54	316.67	316.67	317.54
2003	317.64	318.26	317.31	317.31	318.26
2004	318.24	318.99	317.99	317.99	318.99



2005	318.98	319.71	318.83	318.83	319.71
2006	319.93	320.39	319.58	319.58	320.39
2007	320.59	321.16	320.34	320.34	321.16
2008	321.54	322.11	321.45	321.45	322.11
2009	322.24	322.91	322.22	322.22	322.91
2010	323.04	323.77	323.08	323.04	323.77
2011	324.21	324.68	324.09	324.09	324.68
2012	325.01	325.65	324.99	324.99	325.65
2013	325.92	326.61	325.89	325.89	326.61
2014	327.06	327.66	326.93	326.93	327.66
2015	328.13	328.52	327.99	327.99	328.52
2016	328.94	329.36	328.77	328.77	329.36
2017	329.75	330.37	329.68	329.68	330.37
2018	330.87	331.53	330.90	330.87	331.53
2019	331.85	332.35	331.66	331.66	332.35
2020	333.06	333.48	332.70	332.70	333.48
2021	334.33	334.81	334.03	334.03	334.81
2022	335.71	336.09	335.57	335.57	336.09

1009

1010 **Table S5: Uncertainty in future projections of atmospheric N<sub>2</sub>O dry mole fraction.**

ppb	SSP1-1.9		SSP1-2.6		SSP2-4.5		SSP3-7.0		SSP4-3.4		SSP4-6.0		SSP5-8.5	
Year	Min	Max	Min	Max	Min	Max	Min	Max	Min	Max	Min	Max	Min	Max
2020	330.4	331.1	330.4	331.1	331.0	331.6	331.4	332.0	331.2	331.5	331.2	331.4	331.2	331.9
2030	335.1	336.9	335.5	337.0	337.6	339.6	339.5	342.2	337.5	338.6	338.8	339.6	339.5	341.1
2040	336.2	341.1	336.8	342.0	343.2	347.3	347.9	353.4	340.5	345.7	346.3	349.2	349.2	350.7
2050	336.2	344.6	337.8	345.7	348.5	354.3	356.1	364.9	343.3	353.3	353.5	359.2	359.4	361.2

1011

1012 **References:**

1013

1014 Adalibieke, W., Cui X.Q., Cai H.W., You L.Z., and Zhou F.: Global crop-specific nitrogen fertilization  
 1015 dataset in 1961-2020, *Scientific Data* 10, 617, 2023, <https://www.nature.com/articles/s41597-023-02526-z>

1016 Asaadi, A., and Arora, V. K.: Implementation of nitrogen cycle in the CLASSIC land model,  
 1017 *Biogeosciences*, 18(2), 669-706, 2021.

1018 Aumont, O., Éthé, C., Tagliabue, A., Bopp, L., and Gehlen, M.: PISCES-v2: an ocean biogeochemical  
 1019 model for carbon and ecosystem studies, *Geoscientific Model Development Discussions*, 8(2), 1375-1509,  
 1020 2015.

- 1021 Battaglia, G., and Joos, F.: Marine N<sub>2</sub>O emissions from nitrification and denitrification constrained by  
 1022 modern observations and projected in multimillennial global warming simulations, *Global Biogeochemical*  
 1023 *Cycles*, 32(1), 92-121, 2018.
- 1024 Beaulieu, J. J., Tank, J. L., Hamilton, S. K., Wollheim, W. M., Hall Jr, R. O., Mulholland, P. J., Peterson,  
 1025 B. J., Ashkenas, L. R., Cooper, L. W., and Dahm, C. N. : Nitrous oxide emission from denitrification in  
 1026 stream and river networks, *Proceedings of the National Academy of Sciences*, 108(1), 214-219, 2011.
- 1027 Berdanier, A. B., and Conant, R. T.: Regionally differentiated estimates of cropland N<sub>2</sub>O emissions reduce  
 1028 uncertainty in global calculations, *Global Change Biology*, 18(3), 928-935, 2012.
- 1029 Berthet, S., Jouanno, J., S  f  rian, R., Gehlen, M., and Llovel, W.: How does the phytoplankton–light  
 1030 feedback affect the marine N<sub>2</sub>O inventory?, *Earth System Dynamics*, 14(2), 399-412, 2023.
- 1031 Berthet, S., S  f  rian, R., Bricaud, C., Chevallier, M., Voldoire, A., and Eth  , C.: Evaluation of an online  
 1032 grid-coarsening algorithm in a global eddy-admitting ocean biogeochemical model, *Journal of Advances in*  
 1033 *Modeling Earth Systems*, 11(6), 1759-1783, 2019.
- 1034 Bouwman, A. F., Beusen, A. H. W., and Billen, G. : Human alteration of the global nitrogen and phosphorus  
 1035 soil balances for the period 1970–2050, *Global Biogeochemical Cycles*, 23(4), 2009.
- 1036 Bouwman, A. F., Beusen, A. H. W., Overbeek, C. C., Bureau, D. P., Pawlowski, M., and Glibert, P. M.:  
 1037 Hindcasts and future projections of global inland and coastal nitrogen and phosphorus loads due to finfish  
 1038 aquaculture, *Reviews in Fisheries Science*, 21(2), 112-156, 2013.
- 1039 Bouwman, A. F., Paw  owski, M., Liu, C., Beusen, A. H. W., Shumway, S. E., Glibert, P. M., and Overbeek,  
 1040 C. C.: Global hindcasts and future projections of coastal nitrogen and phosphorus loads due to shellfish and  
 1041 seaweed aquaculture, *Reviews in Fisheries Science*, 19(4), 331-357, 2011.
- 1042 Buendia, E., Tanabe, K., Kranjc, A., Baasansuren, J., Fukuda, M., Ngarize, S., Osako, A., Pyrozhenko, Y.,  
 1043 Shermanau, P., and Federici, S.: 2019 Refinement to the 2006 IPCC Guidelines for National Greenhouse  
 1044 Gas Inventories *Rep.*, 2019.
- 1045 Buitenhuis, E. T., Suntharalingam, P., and Le Qu  r  , C.: Constraints on global oceanic emissions of N<sub>2</sub>O  
 1046 from observations and models, *Biogeosciences*, 15(7), 2161-2175, 2018.
- 1047 Carroll, D., Menemenlis, D., Adkins, J. F., Bowman, K. W., Brix, H., Dutkiewicz, S., Fenty, I., Gierach,  
 1048 M. M., Hill, C., and Jahn, O.: The ECCO-Darwin data-assimilative global ocean biogeochemistry model:  
 1049 Estimates of seasonal to multidecadal surface ocean pCO<sub>2</sub> and air-sea CO<sub>2</sub> flux, *Journal of Advances in*  
 1050 *Modeling Earth Systems*, 12(10), e2019MS001888, 2020.
- 1051 Chatskikh, D., Olesen, J. E., Berntsen, J., Regina, K., and Yamulki, S.: Simulation of effects of soils, climate  
 1052 and management on N<sub>2</sub>O emission from grasslands, *Biogeochemistry*, 76, 395-419, 2005.
- 1053 Crippa, M., Solazzo, E., Guizzardi, D., Monforti-Ferrario, F., Tubiello, F. N., and Leip, A.: Food systems  
 1054 are responsible for a third of global anthropogenic GHG emissions, *Nature Food*, 2(3), 198-209, 2021.
- 1055 Crippa, M., Solazzo, E., Guizzardi, D., Van Dingenen, R., and Leip, A.: Air pollutant emissions from global  
 1056 food systems are responsible for environmental impacts, crop losses and mortality, *Nature Food*, 1-15,  
 1057 2022.
- 1058 Cui, X., Zhou, F., Ciais, P., Davidson, E. A., Tubiello, F. N., Niu, X., Ju, X., Canadell, J. G., Bouwman, A.  
 1059 F., and Jackson, R. B.: Global mapping of crop-specific emission factors highlights hotspots of nitrous  
 1060 oxide mitigation, *Nature Food*, 2(11), 886-893, 2021.
- 1061 Davidson, E. A., de Carvalho, C. J. R., Figueira, A. M., Ishida, F. Y., Ometto, J. P. H. B., Nardoto, G. B.,  
 1062 Sab  , R. T., Hayashi, S. N., Leal, E. C., and Vieira, I. C. G.: Recuperation of nitrogen cycling in Amazonian  
 1063 forests following agricultural abandonment, *Nature*, 447(7147), 995-998, 2007.

1064 Davidson, E. A., Keller, M., Erickson, H. E., Verchot, L. V., and Veldkamp, E.: Testing a conceptual model  
1065 of soil emissions of nitrous and nitric oxides: using two functions based on soil nitrogen availability and  
1066 soil water content, the hole-in-the-pipe model characterizes a large fraction of the observed variation of  
1067 nitric oxide and nitrous oxide emissions from soils, *Bioscience*, 50(8), 667-680, 2000.

1068 Decock, C.: Mitigating nitrous oxide emissions from corn cropping systems in the midwestern US: Potential  
1069 and data gaps, *Environmental Science & Technology*, 48(8), 4247-4256, 2014.

1070 Deemer, B. R., Harrison, J. A., Li, S., Beaulieu, J. J., DelSontro, T., Barros, N., Bezerra-Neto, J. F., Powers,  
1071 S. M., Dos Santos, M. A., and Vonk, J. A.: Greenhouse gas emissions from reservoir water surfaces: a new  
1072 global synthesis, *BioScience*, 66(11), 949-964, 2016.

1073 Del Grosso, S. J., Parton, W. J., Mosier, A. R., Ojima, D. S., Kulmala, A. E., and Phongpan, S.: General  
1074 model for N<sub>2</sub>O and N<sub>2</sub> gas emissions from soils due to denitrification, *Global biogeochemical cycles*, 14(4),  
1075 1045-1060, 2000.

1076 Döll, P., and Lehner, B.: Validation of a new global 30-min drainage direction map, *Journal of Hydrology*,  
1077 258(1-4), 214-231, 2002.

1078 Dürr, H. H., Laruelle, G. G., van Kempen, C. M., Slomp, C. P., Meybeck, M., and Middelkoop, H.:  
1079 Worldwide typology of nearshore coastal systems: defining the estuarine filter of river inputs to the oceans,  
1080 *Estuaries Coasts*, 34, 441-458, 2011.

1081 Eggleston, H. S., Buendia, L., Miwa, K., Ngara, T., and Tanabe, K. : 2006 IPCC guidelines for national  
1082 greenhouse gas inventories, 2006.

1083 FAO (2020), FAO Fisheries and Aquaculture - FishStatJ - Software for Fishery and Aquaculture Statistical  
1084 Time Series. In: FAO Fisheries and Aquaculture Division [online]. Rome. [Cited 3 November 2021]. ,  
1085 edited.

1086 FAO (2022), FAOSTAT Climate Change, Emissions, Emissions Totals, edited.

1087 Ganesan, A. L., Manizza, M., Morgan, E. J., Harth, C. M., Kozlova, E., Lueker, T., Manning, A. J., Lunt,  
1088 M. F., Mühle, J., and Lavric, J. V.: Marine nitrous oxide emissions from three Eastern Boundary Upwelling  
1089 Systems inferred from atmospheric observations, *Geophysical Research Letters*, 47(14), e2020GL087822,  
1090 2020.

1091 Goldewijk, K. K., Beusen, A., Doelman, J., and Stehfest, E.: Anthropogenic land use estimates for the  
1092 Holocene–HYDE 3.2, *Earth System Science Data*, 9(2), 927-953, 2017.

1093 Hall, B. D., Dutton, G. S., and Elkins, J. W.: The NOAA nitrous oxide standard scale for atmospheric  
1094 observations, *Journal of Geophysical Research: Atmospheres*, 112(D9), 2007.

1095 Harris, I. P. D. J., Jones, P. D., Osborn, T. J., and Lister, D. H.: Updated high-resolution grids of monthly  
1096 climatic observations—the CRU TS3. 10 Dataset, *International journal of climatology*, 34(3), 623-642,  
1097 2014.

1098 Heinen, M.: Simplified denitrification models: overview and properties, *Geoderma*, 133(3-4), 444-463,  
1099 2006.

1100 Helgason, B. L., Janzen, H. H., Chantigny, M. H., Drury, C. F., Ellert, B. H., Gregorich, E. G., Lemke, R.  
1101 L., Pattey, E., Rochette, P., and Wagner-Riddle, C.: Toward improved coefficients for predicting direct  
1102 N<sub>2</sub>O emissions from soil in Canadian agroecosystems, *Nutrient Cycling in Agroecosystems*, 72, 87-99,  
1103 2005.

1104 Hénault, C., Bizouard, F., Laville, P., Gabrielle, B., Nicoulaud, B., Germon, J. C., and Cellier, P.:  
1105 Predicting in situ soil N<sub>2</sub>O emission using NOE algorithm and soil database, *Global Change Biology*, 11(1),  
1106 115-127, 2005.

1107 Hersbach, H., Bell, B., Berrisford, P., Hirahara, S., Horányi, A., Muñoz-Sabater, J., Nicolas, J., Peubey, C.,  
1108 Radu, R., and Schepers, D.: Complete ERA5 from 1979: Fifth generation of ECMWF atmospheric  
1109 reanalyses of the global climate, *Copernicus Climate Change Service Data Store*, 2017.

1110 Hickman, J. E., Scholes, R. J., Rosenstock, T. S., Garcia-Pando, C. P., and Nyamangara, J.: Assessing non-  
1111 CO<sub>2</sub> climate-forcing emissions and mitigation in sub-Saharan Africa, *Current Opinion in Environmental*  
1112 *Sustainability*, 9, 65-72, 2014.

1113 Hu, M., Chen, D., and Dahlgren, R. A.: Modeling nitrous oxide emission from rivers: a global assessment,  
1114 *Global Change Biology*, 22(11), 3566-3582, 2016.

1115 Huang, Y., and Gerber, S.: Global soil nitrous oxide emissions in a dynamic carbon-nitrogen model,  
1116 *Biogeosciences*, 12(21), 6405-6427, 2015.

1117 Hurtt, G. C., Chini, L., Sahajpal, R., Frohking, S., Boudris, B. L., Calvin, K., Doelman, J. C., Fisk, J.,  
1118 Fujimori, S., and Klein Goldewijk, K.: Harmonization of global land use change and management for the  
1119 period 850–2100 (LUH2) for CMIP6, *Geoscientific Model Development*, 13(11), 5425-5464, 2020.

1120 IEA: World Energy Outlook 2021*Rep.*, IEA, Paris, 2021.

1121 Inatomi, M., Ito, A., Ishijima, K., and Murayama, S.: Greenhouse gas budget of a cool-temperate deciduous  
1122 broad-leaved forest in Japan estimated using a process-based model, *Ecosystems*, 13, 472-483, 2010.

1123 IPCC: Revised 1996 IPCC Guidelines for National Greenhouse Gas Inventories, 1996.

1124 IPCC: Good practice guidance and uncertainty management in national greenhouse gas inventories, 2000.

1125 IPCC: IPCC Guidelines for National Greenhouse Gas Inventories*Rep.*, Hayama, Japan, 2006.

1126 Ito, A., Nishina, K., Ishijima, K., Hashimoto, S., and Inatomi, M.: Emissions of nitrous oxide (N<sub>2</sub>O) from  
1127 soil surfaces and their historical changes in East Asia: a model-based assessment, *Progress in Earth*  
1128 *Planetary Science*, 5, 1-13, 2018.

1129 Janssens-Maenhout, G., Crippa, M., Guizzardi, D., Muntean, M., Schaaf, E., Dentener, F., Bergamaschi,  
1130 P., Pagliari, V., Olivier, J. G., and Peters, J. A.: EDGAR v4. 3.2 Global Atlas of the three major greenhouse  
1131 gas emissions for the period 1970–2012, *Earth System Science Data*, 11(3), 959-1002, 2019.

1132 Jin, X., and Gruber, N.: Offsetting the radiative benefit of ocean iron fertilization by enhancing N<sub>2</sub>O  
1133 emissions, *Geophysical research letters*, 30(24), 2003.

1134 Johnson, D. J., Niedbalski, N. P., Ervin, J. S., and Patnaik, S. S.: Ammonium carbamate-based heat  
1135 exchanger reactor as an endothermic heat sink for thermal management, *International Journal of Heat Mass*  
1136 *Transfer*, 91, 766-776, 2015.

1137 Kalnay, E., Kanamitsu, M., Kistler, R., Collins, W., Deaven, D., Gandin, L., Iredell, M., Saha, S., White,  
1138 G., and Woollen, J.: The NCEP/NCAR 40-year reanalysis project, *Bulletin of the American meteorological*  
1139 *Society*, 77(3), 437-472, 1996.

1140 Keller, M., and Reiners, W. A.: Soil-atmosphere exchange of nitrous oxide, nitric oxide, and methane under  
1141 secondary succession of pasture to forest in the Atlantic lowlands of Costa Rica, *Global Biogeochemical*  
1142 *Cycles*, 8(4), 399-409, 1994.

1143 Kim, D.-G., Giltrap, D., and Hernandez-Ramirez, G.: Background nitrous oxide emissions in agricultural  
1144 and natural lands: a meta-analysis, *Plant Soil*, 373, 17-30, 2013a.

1145 Kim, D.-G., Hernandez-Ramirez, G., and Giltrap, D.: Linear and nonlinear dependency of direct nitrous  
1146 oxide emissions on fertilizer nitrogen input: A meta-analysis, *Agriculture, Ecosystems Environment*, 168,  
1147 53-65, 2013b.

- 1148 Kock, A., and Bange, H. W.: Counting the ocean's greenhouse gas emissions, *Eos: Earth Space Science*  
 1149 *News*, 96(3), 10-13, 2015.
- 1150 Kou Giesbrecht, S., and Arora, V. K.: Representing the dynamic response of vegetation to nitrogen  
 1151 limitation via biological nitrogen fixation in the CLASSIC Land Model, *Global Biogeochemical Cycles*,  
 1152 36(6), e2022GB007341, 2022.
- 1153 Landolfi, A., Somes, C. J., Koeve, W., Zamora, L. M., and Oschlies, A.: Oceanic nitrogen cycling and N<sub>2</sub>O  
 1154 flux perturbations in the Anthropocene, *Global Biogeochemical Cycles*, 31(8), 1236-1255, 2017.
- 1155 Laruelle, G. G., Landschützer, P., Gruber, N., Tison, J.-L., Delille, B., and Regnier, P.: Global high-  
 1156 resolution monthly pCO<sub>2</sub> climatology for the coastal ocean derived from neural network interpolation,  
 1157 *Biogeosciences*, 14(19), 4545-4561, 2017.
- 1158 Lauerwald, R., Regnier, P., Figueiredo, V., Enrich-Prast, A., Bastviken, D., Lehner, B., Maavara, T., and  
 1159 Raymond, P.: Natural lakes are a minor global source of N<sub>2</sub>O to the atmosphere, *Global Biogeochemical*  
 1160 *Cycles*, 33(12), 1564-1581, 2019.
- 1161 Le Quéré, C., Buitenhuis, E. T., Moriarty, R., Alvain, S., Aumont, O., Bopp, L., Chollet, S., Enright, C.,  
 1162 Franklin, D. J., and Geider, R. J.: Role of zooplankton dynamics for Southern Ocean phytoplankton biomass  
 1163 and global biogeochemical cycles, *Biogeosciences*, 13(14), 4111-4133, 2016.
- 1164 Lehner, B., Liermann, C. R., Revenga, C., Vörösmarty, C., Fekete, B., Crouzet, P., Döll, P., Endejan, M.,  
 1165 Frenken, K., and Magome, J. : High-resolution mapping of the world's reservoirs and dams for sustainable  
 1166 river-flow management, *Frontiers in Ecology the Environment*, 9(9), 494-502, 2011.
- 1167 Lehner, B., Verdin, K., and Jarvis, A.: New global hydrography derived from spaceborne elevation data,  
 1168 *Eos, Transactions American Geophysical Union*, 89(10), 93-94, 2008.
- 1169 Lehuger, S., Gabrielle, B., Laville, P., Lamboni, M., Loubet, B., and Cellier, P.: Predicting and mitigating  
 1170 the net greenhouse gas emissions of crop rotations in Western Europe, *Agricultural Forest Meteorology*,  
 1171 151(12), 1654-1671, 2011.
- 1172 Leppelt, T., Dechow, R., Gebbert, S., Freibauer, A., Lohila, A., Augustin, J., Drösler, M., Fiedler, S.,  
 1173 Glatzel, S., and Höper, H.: Nitrous oxide emission budgets and land-use-driven hotspots for organic soils  
 1174 in Europe, *Biogeosciences*, 11(23), 6595-6612, 2014.
- 1175 Lan, X., E.J. Dlugokencky, J.W. Mund, A.M. Crotwell, M.J. Crotwell, E. Moglia, M. Madronich, D. Neff  
 1176 and K.W. Thoning (2022), Atmospheric Nitrous Oxide Dry Air  
 1177 Mole Fractions from the NOAA GML Carbon Cycle Cooperative Global Air Sampling Network,  
 1178 1997-2021, Version: 2022-11-21, <https://doi.org/10.15138/53g1-x417>
- 1179 Li, C., Aber, J., Stange, F., Butterbach-Bahl, K., and Papen, H.: A process-oriented model of N<sub>2</sub>O and NO  
 1180 emissions from forest soils: 1. Model development, *Journal of Geophysical Research: Atmospheres*,  
 1181 105(D4), 4369-4384, 2000.
- 1182 Li, C., Frohling, S., and Frohling, T. A.: A model of nitrous oxide evolution from soil driven by rainfall  
 1183 events: 2. Model applications, *Journal of Geophysical Research: Atmospheres*, 97(D9), 9777-9783, 1992.
- 1184 Liang, J. H., Deutsch, C., McWilliams, J. C., Baschek, B., Sullivan, P. P., and Chiba, D.: Parameterizing  
 1185 bubble-mediated air-sea gas exchange and its effect on ocean ventilation, *Global Biogeochemical Cycles*,  
 1186 27(3), 894-905, 2013.
- 1187 Lu, C., and Tian, H.: Net greenhouse gas balance in response to nitrogen enrichment: perspectives from a  
 1188 coupled biogeochemical model, *Global Change Biology*, 19(2), 571-588, 2013.
- 1189 Maavara, T., Lauerwald, R., Laruelle, G. G., Akbarzadeh, Z., Bouskill, N. J., Van Cappellen, P., and  
 1190 Regnier, P.: Nitrous oxide emissions from inland waters: Are IPCC estimates too high?, *Global Change*  
 1191 *Biology*, 25(2), 473-488, 2019.

- 1192 Madec, G.: NEMO ocean engine: Note du pole de modélisation, Institut Pierre-Simon Laplace (IPSL),  
1193 France, No 27 ISSN No 1288-1619, *France: IPSL*, 2008.
- 1194 Madec, G., Bourdallé-Badie, R., Bouttier, P.-A., Bricaud, C., Bruciaferri, D., Calvert, D., Chanut, J.,  
1195 Clementi, E., Coward, A., and Delrosso, D.: NEMO ocean engine, 2017.
- 1196 Manizza, M., Menemenlis, D., Zhang, H., and Miller, C. E.: Modeling the recent changes in the Arctic  
1197 Ocean CO<sub>2</sub> sink (2006–2013), *Global Biogeochemical Cycles*, 33(3), 420-438, 2019.
- 1198 Manizza, M., Carroll, D., Menemenlis, D., Zhang, H., & Miller, C. E.: Modeling the recent changes of  
1199 phytoplankton blooms dynamics in the Arctic Ocean. *Journal of Geophysical Research: Oceans*, 128,  
1200 e2022JC019152, 2023.
- 1201 Martinez-Rey, J., Bopp, L., Gehlen, M., Tagliabue, A., and Gruber, N.: Projections of oceanic N<sub>2</sub>O  
1202 emissions in the 21st century using the IPSL Earth system model, *Biogeosciences*, 12(13), 4133-4148, 2015.
- 1203 Marzadri, A., Amatulli, G., Tonina, D., Bellin, A., Shen, L. Q., Allen, G. H., and Raymond, P. A.: Global  
1204 riverine nitrous oxide emissions: The role of small streams and large rivers, *Science of The Total  
1205 Environment*, 776, 145148, 2021.
- 1206 Marzadri, A., Dee, M. M., Tonina, D., Bellin, A., and Tank, J. L.: Role of surface and subsurface processes  
1207 in scaling N<sub>2</sub>O emissions along riverine networks, *Proceedings of the National Academy of Sciences*,  
1208 114(17), 4330-4335, 2017.
- 1209 McCrackin, M. L., Harrison, J. A., and Compton, J. E.: Factors influencing export of dissolved inorganic  
1210 nitrogen by major rivers: A new, seasonal, spatially explicit, global model, *Global Biogeochemical Cycles*,  
1211 28(3), 269-285, 2014.
- 1212 Melillo, J. M., Steudler, P. A., Feigl, B. J., Neill, C., Garcia, D., Piccolo, M. C., Cerri, C. C., and Tian, H.:  
1213 Nitrous oxide emissions from forests and pastures of various ages in the Brazilian Amazon, *Journal of  
1214 Geophysical Research: Atmospheres*, 106(D24), 34179-34188, 2001.
- 1215 Messenger, M. L., Lehner, B., Grill, G., Nedeva, I., and Schmitt, O.: Estimating the volume and age of water  
1216 stored in global lakes using a geo-statistical approach, *Nature Communications*, 7(1), 13603, 2016.
- 1217 Nevison, C., Butler, J. H., and Elkins, J. W.: Global distribution of N<sub>2</sub>O and the ΔN<sub>2</sub>O-AOU yield in the  
1218 subsurface ocean, *Global Biogeochemical Cycles*, 17(4), 2003.
- 1219 Pan, S., Bian, Z., Tian, H., Yao, Y., Najjar, R. G., Friedrichs, M. A. M., Hofmann, E. E., Xu, R., and Zhang,  
1220 B.: Impacts of multiple environmental changes on long-term nitrogen loading from the Chesapeake Bay  
1221 watershed, *Journal of Geophysical Research: Biogeosciences*, 126(5), e2020JG005826, 2021.
- 1222 Parekh, P., Joos, F., and Müller, S. A.: A modeling assessment of the interplay between aeolian iron fluxes  
1223 and iron-binding ligands in controlling carbon dioxide fluctuations during Antarctic warm events,  
1224 *Paleoceanography*, 23(4), 2008.
- 1225 Parton, W. J., Mosier, A. R., Ojima, D. S., Valentine, D. W., Schimel, D. S., Weier, K., and Kulmala, A.  
1226 E.: Generalized model for N<sub>2</sub> and N<sub>2</sub>O production from nitrification and denitrification, *Global  
1227 biogeochemical cycles*, 10(3), 401-412, 1996.
- 1228 Patra, P. K., Dlugokencky, E. J., Elkins, J. W., Dutton, G. S., Tohjima, Y., Sasakawa, M., Ito, A., Weiss,  
1229 R. F., Manizza, M., and Krummel, P. B.: Forward and inverse modelling of atmospheric nitrous oxide using  
1230 MIROC4-atmospheric chemistry-transport model, *Journal of the Meteorological Society of Japan. Ser. II*,  
1231 100(2), 361-386, 2022.
- 1232 Patra, P. K., Takigawa, M., Watanabe, S., Chandra, N., Ishijima, K., and Yamashita, Y.: Improved chemical  
1233 tracer simulation by MIROC4. 0-based atmospheric chemistry-transport model (MIROC4-ACTM), *Sola*,  
1234 14, 91-96, 2018.

- 1235 Paulot, F., Jacob, D. J., Johnson, M. T., Bell, T. G., Baker, A. R., Keene, W. C., Lima, I. D., Doney, S. C.,  
 1236 and Stock, C. A.: Global oceanic emission of ammonia: Constraints from seawater and atmospheric  
 1237 observations, *Global Biogeochemical Cycles*, 29(8), 1165-1178, 2015.
- 1238 Peltier, W. R.: Global glacial isostasy and the surface of the ice-age Earth: the ICE-5G (VM2) model and  
 1239 GRACE, *Annual Review of Earth and Planetary Sciences*, 32, 111-149, 2004.
- 1240 Portmann, F. T., Siebert, S., and Döll, P.: MIRCA2000—Global monthly irrigated and rainfed crop areas  
 1241 around the year 2000: A new high-resolution data set for agricultural and hydrological modeling, *Global*  
 1242 *Biogeochemical Cycles*, 24(1), 2010.
- 1243 Porwollik, V., Rolinski, S., Heinke, J., and Müller, C.: Generating a rule-based global gridded tillage  
 1244 dataset, *Earth System Science Data*, 11(2), 823-843, 2019.
- 1245 Prather, M. J., Hsu, J., DeLuca, N. M., Jackman, C. H., Oman, L. D., Douglass, A. R., Fleming, E. L.,  
 1246 Strahan, S. E., Steenrod, S. D., and Søvde, O. A.: Measuring and modeling the lifetime of nitrous oxide  
 1247 including its variability, *Journal of Geophysical Research: Atmospheres*, 120(11), 5693-5705, 2015.
- 1248 Resplandy, L., Hogikyan, A., Müller, J. D., Najjar, R. G., Bange, H. W., Bianchi, D., et al.: A synthesis of  
 1249 global coastal ocean greenhouse gas fluxes. *Global Biogeochemical Cycles*, 38, e2023GB007803, 2024.
- 1250 Rochette, P., and Janzen, H. H.: Towards a revised coefficient for estimating N<sub>2</sub>O emissions from legumes,  
 1251 *Nutrient Cycling in Agroecosystems*, 73, 171-179, 2005.
- 1252 Rosentreter, J. A., Laruelle, G. G., Bange, H. W., Bianchi, T. S., Busecke, J. J. M., Cai, W.-J., Eyre, B. D.,  
 1253 Forbrich, I., Kwon, E. Y., and Maavara, T.: Coastal vegetation and estuaries are collectively a greenhouse  
 1254 gas sink, *Nature Climate Change*, 1-9, 2023.
- 1255 Sacks, W. J., Deryng, D., Foley, J. A., and Ramankutty, N.: Crop planting dates: an analysis of global  
 1256 patterns, *Global Ecology Biogeography*, 19(5), 607-620, 2010.
- 1257 Salas y Méliá, D.: A global coupled sea ice–ocean model, *Ocean Modelling*, 4(2), 137-172, 2002.
- 1258 Séférian, R., Nabat, P., Michou, M., Saint-Martin, D., Voltaire, A., Colin, J., Decharme, B., Delire, C.,  
 1259 Berthet, S., and Chevallier, M.: Evaluation of CNRM Earth System Model, CNRM-ESM2-1: role of Earth  
 1260 system processes in present-day and future climate, *Journal of Advances in Modeling Earth Systems*,  
 1261 11(12), 4182-4227, 2019.
- 1262 Shangguan, W., Dai, Y., Duan, Q., Liu, B., and Yuan, H.: A global soil data set for earth system modeling,  
 1263 *Journal of Advances in Modeling Earth Systems*, 6(1), 249-263, 2014.
- 1264 Shcherbak, I., Millar, N., and Robertson, G. P.: Global metaanalysis of the nonlinear response of soil nitrous  
 1265 oxide (N<sub>2</sub>O) emissions to fertilizer nitrogen, *Proceedings of the National Academy of Sciences*, 111(25),  
 1266 9199-9204, 2014.
- 1267 Shu, S., Jain, A. K., Koven, C. D., and Mishra, U.: Estimation of permafrost SOC stock and turnover time  
 1268 using a land surface model with vertical heterogeneity of permafrost soils, *Global Biogeochemical Cycles*,  
 1269 34(11), e2020GB006585, 2020.
- 1270 Solazzo, E., Crippa, M., Guizzardi, D., Muntean, M., Choulga, M., and Janssens-Maenhout, G.:  
 1271 Uncertainties in the Emissions Database for Global Atmospheric Research (EDGAR) emission inventory  
 1272 of greenhouse gases, *Atmospheric Chemistry Physics*, 21(7), 5655-5683, 2021.
- 1273 Stehfest, E., and Bouwman, L.: N<sub>2</sub>O and NO emission from agricultural fields and soils under natural  
 1274 vegetation: summarizing available measurement data and modeling of global annual emissions, *Nutrient*  
 1275 *cycling in agroecosystems*, 74, 207-228, 2006.

- 1276 Sullivan, B. W., Nifong, R. L., Nasto, M. K., Alvarez-Clare, S., Dencker, C. M., Soper, F. M., Shoemaker,  
1277 K. T., Ishida, F. Y., Zaragoza-Castells, J., and Davidson, E. A.: Biogeochemical recuperation of lowland  
1278 tropical forest during succession, *Ecology*, *100*(4), e02641, 2019.
- 1279 Tarantola, A.: *Inverse problem theory and methods for model parameter estimation*, SIAM, 2005.
- 1280 Thompson, R. L., Chevallier, F., Crotwell, A. M., Dutton, G., Langenfelds, R. L., Prinn, R. G., Weiss, R.  
1281 F., Tohjima, Y., Nakazawa, T., and Krummel, P. B.: Nitrous oxide emissions 1999 to 2009 from a global  
1282 atmospheric inversion, *Atmospheric Chemistry Physics*, *14*(4), 1801-1817, 2014.
- 1283 Thornton, P. E., and Rosenbloom, N. A. : Ecosystem model spin-up: Estimating steady state conditions in  
1284 a coupled terrestrial carbon and nitrogen cycle model, *Ecological Modelling*, *189*(1-2), 25-48, 2005.
- 1285 Tian, H., Bian, Z., Shi, H., Qin, X., Pan, N., Lu, C., Pan, S., Tubiello, F. N., Chang, J., and Conchedda, G.:  
1286 History of anthropogenic Nitrogen inputs (HaNi) to the terrestrial biosphere: a 5 arcmin resolution annual  
1287 dataset from 1860 to 2019, *Earth System Science Data*, *14*(10), 4551-4568, 2022.
- 1288 Tian, H., Chen, G., Zhang, C., Liu, M., Sun, G., Chappelka, A., Ren, W., Xu, X., Lu, C., and Pan, S.:  
1289 Century-scale responses of ecosystem carbon storage and flux to multiple environmental changes in the  
1290 southern United States, *Ecosystems*, *15*, 674-694, 2012a.
- 1291 Tian, H., Lu, C., Chen, G., Tao, B., Pan, S., Grosso, S. J. D., Xu, X., Bruhwiler, L., Wofsy, S. C., and Kort,  
1292 E. A.: Contemporary and projected biogenic fluxes of methane and nitrous oxide in North American  
1293 terrestrial ecosystems, *Frontiers in Ecology the Environment*, *10*(10), 528-536, 2012b.
- 1294 Tian, H., Ren, W., Yang, J., Tao, B., Cai, W. J., Lohrenz, S. E., Hopkinson, C. S., Liu, M., Yang, Q., and  
1295 Lu, C. : Climate extremes dominating seasonal and interannual variations in carbon export from the  
1296 Mississippi River Basin, *Global Biogeochemical Cycles*, *29*(9), 1333-1347, 2015.
- 1297 Tian, H., Xu, R., Canadell, J. G., Thompson, R. L., Winiwarter, W., Suntharalingam, P., Davidson, E. A.,  
1298 Ciais, P., Jackson, R. B., Janssens-Maenhout, G., ..., and Yuanzhi, Y.: A comprehensive quantification of  
1299 global nitrous oxide sources and sinks, *Nature*, *586*(7828), 248-256, 2020a.
- 1300 Tian, H., Xu, R., Pan, S., Yao, Y., Bian, Z., Cai, W. J., Hopkinson, C. S., Justic, D., Lohrenz, S., and Lu,  
1301 C.: Long-term trajectory of nitrogen loading and delivery from Mississippi River Basin to the Gulf of  
1302 Mexico, *Global Biogeochemical Cycles*, *34*(5), e2019GB006475, 2020b.
- 1303 Tian, H., Xu, X., Liu, M., Ren, W., Zhang, C., Chen, G., and Lu, C.: Spatial and temporal patterns of CH<sub>4</sub>  
1304 and N<sub>2</sub>O fluxes in terrestrial ecosystems of North America during 1979–2008: application of a global  
1305 biogeochemistry model, *Biogeosciences*, *7*(9), 2673-2694, 2010.
- 1306 Tian, H., Xu, X., Lu, C., Liu, M., Ren, W., Chen, G., Melillo, J., and Liu, J.: Net exchanges of CO<sub>2</sub>, CH<sub>4</sub>,  
1307 and N<sub>2</sub>O between China's terrestrial ecosystems and the atmosphere and their contributions to global  
1308 climate warming, *Journal of Geophysical Research: Biogeosciences*, *116*(G2), 2011.
- 1309 Tian, H., Yang, J., Lu, C., Xu, R., Canadell, J. G., Jackson, R. B., Arneeth, A., Chang, J., Chen, G., and  
1310 Ciais, P.: The global N<sub>2</sub>O model intercomparison project, *Bulletin of the American Meteorological Society*,  
1311 *99*(6), 1231-1251, 2018.
- 1312 Tian, H., R. Xu, S. Pan, Y. Yao, Z. Bian, W. J. Cai, C. S. Hopkinson, D. Justic, S. Lohrenz, C. Lu, W. Ren,  
1313 and J. Yang. (2020). Long-Term Trajectory of Nitrogen Loading and Delivery From Mississippi River  
1314 Basin to the Gulf of Mexico. *Global Biogeochemical Cycles*, *34*(5), e2019GB006475.  
1315 <https://doi.org/10.1029/2019GB006475>.
- 1316 Tschumi, T., Joos, F., Gehlen, M., and Heinze, C.: Deep ocean ventilation, carbon isotopes, marine  
1317 sedimentation and the deglacial CO<sub>2</sub> rise, *Climate of the Past*, *7*(3), 771-800, 2011.
- 1318 Tsujino, H., Urakawa, L. S., Griffies, S. M., Danabasoglu, G., Adcroft, A. J., Amaral, A. E., Arsouze, T.,  
1319 Bentsen, M., Bernardello, R., and Böning, C. W.: Evaluation of global ocean–sea-ice model simulations



- 1320 based on the experimental protocols of the Ocean Model Intercomparison Project phase 2 (OMIP-2),  
1321 *Geoscientific Model Development*, 13(8), 3643-3708, 2020.
- 1322 Tsujino, H., Urakawa, S., Nakano, H., Small, R. J., Kim, W. M., Yeager, S. G., Danabasoglu, G., Suzuki,  
1323 T., Bamber, J. L., and Bentsen, M.: JRA-55 based surface dataset for driving ocean–sea-ice models (JRA55-  
1324 do), *Ocean Modelling*, 130, 79-139, 2018.
- 1325 Van Drecht, G., Bouwman, A. F., Harrison, J., and Knoop, J. M.: Global nitrogen and phosphate in urban  
1326 wastewater for the period 1970 to 2050, *Global Biogeochemical Cycles*, 23(4), 2009.
- 1327 Van Drecht, G., Bouwman, A. F., Knoop, J. M., Beusen, A. H. W., and Meinardi, C. R.: Global modeling  
1328 of the fate of nitrogen from point and nonpoint sources in soils, groundwater, and surface water, *Global*  
1329 *Biogeochemical Cycles*, 17(4), 2003.
- 1330 Verchot, L. V., Davidson, E. A., Cattânio, H., Ackerman, I. L., Erickson, H. E., and Keller, M.: Land use  
1331 change and biogeochemical controls of nitrogen oxide emissions from soils in eastern Amazonia, *Global*  
1332 *Biogeochemical Cycles*, 13(1), 31-46, 1999.
- 1333 Walter, K., Don, A., Fuß, R., Kern, J., Drewer, J., and Flessa, H.: Direct nitrous oxide emissions from  
1334 oilseed rape cropping—a meta-analysis, *Gcb Bioenergy*, 7(6), 1260-1271, 2015.
- 1335 Wang, Q., Zhou, F., Shang, Z., Ciais, P., Winiwarter, W., Jackson, R. B., Tubiello, F. N., Janssens-  
1336 Maenhout, G., Tian, H., and Cui, X.: Data-driven estimates of global nitrous oxide emissions from  
1337 croplands, *National Science Review*, 7(2), 441–452, 2020.
- 1338 Wanninkhof, R.: Relationship between wind speed and gas exchange over the ocean, *Journal of*  
1339 *Geophysical Research: Oceans*, 97(C5), 7373-7382, 1992.
- 1340 Wanninkhof, R.: Relationship between wind speed and gas exchange over the ocean revisited, *Limnology*  
1341 *Oceanography: Methods*, 12(6), 351-362, 2014.
- 1342 Weiss, R. F., and Price, B. A.: Nitrous oxide solubility in water and seawater, *Marine Chemistry*, 8(4), 347-  
1343 359, 1980.
- 1344 Wells, K. C., Millet, D. B., Bousserrez, N., Henze, D. K., Chaliyakunnel, S., Griffis, T. J., Luan, Y.,  
1345 Dlugokencky, E. J., Prinn, R. G., and O'Doherty, S.: Simulation of atmospheric N<sub>2</sub>O with GEOS-Chem  
1346 and its adjoint: evaluation of observational constraints, *Geoscientific Model Development*, 8(10), 3179-  
1347 3198, 2015.
- 1348 Wilson, C., Chipperfield, M. P., Gloor, M., and Chevallier, F.: Development of a variational flux inversion  
1349 system (INVICAT v1. 0) using the TOMCAT chemical transport model, *Geoscientific Model Development*,  
1350 7(5), 2485-2500, 2014.
- 1351 Wollheim, W. M., Vörösmarty, C. J., Bouwman, A. F., Green, P., Harrison, J., Linder, E., Peterson, B. J.,  
1352 Seitzinger, S. P., and Syvitski, J. P. M.: Global N removal by freshwater aquatic systems using a spatially  
1353 distributed, within-basin approach, *Global Biogeochemical Cycles*, 22(2), 2008.
- 1354 Xu-Ri, and Prentice, I. C.: Terrestrial nitrogen cycle simulation with a dynamic global vegetation model,  
1355 *Global Change Biology*, 14(8), 1745-1764, 2008.
- 1356 Xu, R., Tian, H., Lu, C., Pan, S., Chen, J., Yang, J., and Zhang, B.: Preindustrial nitrous oxide emissions  
1357 from the land biosphere estimated by using a global biogeochemistry model, *Climate of the Past*, 13(7),  
1358 977-990, 2017.
- 1359 Xu, X., Sharma, P., Shu, S., Lin, T.-S., Ciais, P., Tubiello, F. N., Smith, P., Campbell, N., and Jain, A. K.:  
1360 Global greenhouse gas emissions from animal-based foods are twice those of plant-based foods, *Nature*  
1361 *Food*, 2(9), 724-732, 2021.

- 1362 Xu, X., Tian, H., Liu, M., Ren, W., Chen, G., Lu, C., and Zhang, C.: Multiple-factor controls on terrestrial  
1363 N<sub>2</sub>O flux over North America from 1979 through 2010, *Biogeosciences Discussions*, 8(6), 2011.
- 1364 Yang, H., Zhou, F., Piao, S., Huang, M., Chen, A., Ciais, P., Li, Y., Lian, X., Peng, S., and Zeng, Z.:  
1365 Regional patterns of future runoff changes from Earth system models constrained by observation,  
1366 *Geophysical Research Letters*, 44(11), 5540-5549, 2017.
- 1367 Yang, Q., Tian, H., Friedrichs, M. A. M., Hopkinson, C. S., Lu, C., and Najjar, R. G.: Increased nitrogen  
1368 export from eastern North America to the Atlantic Ocean due to climatic and anthropogenic changes during  
1369 1901–2008, *Journal of Geophysical Research: Biogeosciences*, 120(6), 1046-1068, 2015.
- 1370 Yang, S., Chang, B. X., Warner, M. J., Weber, T. S., Bourbonnais, A. M., Santoro, A. E., Kock, A.,  
1371 Sonnerup, R. E., Bullister, J. L., and Wilson, S. T.: Global reconstruction reduces the uncertainty of oceanic  
1372 nitrous oxide emissions and reveals a vigorous seasonal cycle, *Proceedings of the National Academy of  
1373 Sciences*, 117(22), 11954-11960, 2020.
- 1374 Yang, X., Wittig, V., Jain, A. K., and Post, W.: Integration of nitrogen cycle dynamics into the Integrated  
1375 Science Assessment Model for the study of terrestrial ecosystem responses to global change, *Global  
1376 Biogeochemical Cycles*, 23(4), 2009.
- 1377 Yao, Y., Tian, H., Shi, H., Pan, S., Xu, R., Pan, N., and Canadell, J. G.: Increased global nitrous oxide  
1378 emissions from streams and rivers in the Anthropocene, *Nature Climate Change*, 10(2), 138-142, 2020.
- 1379 Yao, Y., Tian, H., Xu, X., Li, Y., and Pan, S.: Dynamics and controls of inland water CH<sub>4</sub> emissions  
1380 across the Conterminous United States: 1860-2019, *Water Research*, 224, 119043, 2022.
- 1381 Yool, A., Martin, A. P., Fernández, C., and Clark, D. R.: The significance of nitrification for oceanic new  
1382 production, *Nature*, 447(7147), 999-1002, 2007.
- 1383 Zaehle, S., Ciais, P., Friend, A. D., and Prieur, V.: Carbon benefits of anthropogenic reactive nitrogen  
1384 offset by nitrous oxide emissions, *Nature Geoscience*, 4(9), 601-605, 2011.
- 1385 Zaehle, S., and Friend, A. D.: Carbon and nitrogen cycle dynamics in the O-CN land surface model: 1.  
1386 Model description, site-scale evaluation, and sensitivity to parameter estimates, *Global Biogeochemical  
1387 Cycles*, 24(1), 2010.
- 1388 Zamora, L. M., and Oschlies, A.: Surface nitrification: A major uncertainty in marine N<sub>2</sub>O emissions,  
1389 *Geophysical Research Letters*, 41(12), 4247-4253, 2014.
- 1390 Zhang, Y., Li, C., Zhou, X., and Moore III, B.: A simulation model linking crop growth and soil  
1391 biogeochemistry for sustainable agriculture, *Ecological Modelling*, 151(1), 75-108, 2002.
- 1392 Zhou, F., Shang, Z., Zeng, Z., Piao, S., Ciais, P., Raymond, P. A., Wang, X., Wang, R., Chen, M., and  
1393 Yang, C.: New model for capturing the variations of fertilizer-induced emission factors of N<sub>2</sub>O, *Global  
1394 Biogeochemical Cycles*, 29(6), 885-897, 2015.
- 1395 Zhou, J. B., Jiang, M. M., and Chen, G. Q.: Estimation of methane and nitrous oxide emission from  
1396 livestock and poultry in China during 1949–2003, *Energy Policy*, 35(7), 3759-3767, 2007.
- 1397 Zhu, Q., Riley, W. J., Tang, J., and Koven, C. D. : Multiple soil nutrient competition between plants,  
1398 microbes, and mineral surfaces: model development, parameterization, and example applications in  
1399 several tropical forests, *Biogeosciences*, 13(1), 341-363, 2016.